JGR Oceans

RESEARCH ARTICLE
10.1029/2018JC014701

New Hydrographic Measurements of the Upper Arctic Western Eurasian Basin in 2017 Reveal Fresher Mixed Layer and Shallower Warm Layer Than 2005–2012 Climatology

Marylou Athanase[1], Nathalie Sennéchael[1], Gilles Garric[2], Zoé Koenig[1], Elisabeth Boles[1], and Christine Provost[1]

[1]Laboratoire LOCEAN-IPSL, Sorbonne Université (UPMC, Université Paris 6), CNRS, IRD, MNHN, Paris, France, [2]Mercator Ocean, Parc Technologique du Canal, Ramonville-Saint-Agne, France

Key Points:

- Autonomous profilers provide an extensive physical and biogeochemical characterization of the western Eurasian Basin upper 350 m in 2017
- The western Eurasian Basin exhibits a fresher surface layer and shallower warm Atlantic Water layer in 2017 than in 2005-2012
- Mercator Ocean operational model outputs bring insights on the observed mesoscale structures in the halocline and warm layer

Correspondence to:
M. Athanase,
mathanase@locean-ipsl.upmc.fr

Citation:
Athanase, M., Sennéchael, N., Garric, G., Koenig, Z., Boles, E., & Provost, C. (2019). New hydrographic measurements of the upper Arctic western Eurasian Basin in 2017 reveal fresher mixed layer and shallower warm layer than 2005–2012 climatology. *Journal of Geophysical Research: Oceans*, *124*. https://doi.org/10.1029/2018JC014701

Received 19 OCT 2018
Accepted 19 JAN 2019
Accepted article online 25 JAN 2019

Abstract In 2017, Ice Atmosphere Ocean Observing System autonomous drifting platforms provided extensive physical and biogeochemical data in the upper 350 m of the western Eurasian Basin through their 8-month drift across the Amundsen Basin, the Gakkel Ridge, the Nansen Basin and western Fram Strait. Comparison with WOA13 climatology indicates a fresher surface layer and shallower warm layer in 2017 than in 2005–2012. The Ice Atmosphere Ocean Observing System 2017 data feature two halocline eddies in the Amundsen Basin and two Atlantic Water (AW) mesoscale structures in the Nansen Basin. Analysis of the global (1/12)° Mercator Ocean operational system suggests that the halocline eddies resulted from instabilities in the frontal zone between fresher Makarov waters and saltier Eurasian waters. This frontal region appears to have shifted further southeast in 2017 (near 88°N, 10°E) compared to 2005–2012. The operational system depicts the large AW structure in the Nansen Basin (140 km crossed as far as 83.7°N, 34.5°E) as an AW meander from the Arctic Circumpolar Boundary Current, which turned into an anticyclonic eddy about a month after the platforms drifted away. The AW structure at 82.8°N, 3°W, northwest of the Yermak Plateau, corresponds to an AW recirculating branch detaching from the Yermak Plateau slope back toward Fram Strait.

Plain Language Summary In 2017, IAOOS (Ice Atmosphere Ocean Observing System) autonomous drifting platforms provided extensive physical and biogeochemical data in the upper 350 m of the Western Eurasian Basin through their 8-month drift. The surface layer is fresher and the warm layer shallower in 2017 than in 2005-2012. The IAOOS 2017 measurements document several medium scale ocean structures. Simulations from a high resolution ((1/12)°) model (Mercator Ocean operational model) provide insights on the nature and origin of these observed structures.

1. Introduction

Over the recent decades, the Arctic has experienced numerous changes; drastic sea ice loss during summers and reduced sea ice thickness and volume are evident signs of global climate change (Carmack et al., 2015; Jeffries et al., 2013; Stroeve et al., 2012). The causes of this sea ice reduction involve a complex combination of changes in the atmospheric and oceanic heat, freshwater, and momentum fluxes (Comiso et al., 2008; Polyakov et al., 2010; Serreze & Barry, 2011). A large part of the Arctic sea ice loss results from summer solar heating of the ocean surface mixed layer through leads in the ice and open water (Perovich et al., 2011). Further decrease of the seasonal ice extent and increase of the open water surface enhance atmospheric forcing onto the ocean and accelerate feedback processes (Carmack et al., 2015; Stroeve et al., 2012).

In most of the Arctic Ocean, the strongly stratified halocline prevents the heat of the warm Atlantic Water (AW) from reaching the surface. One notable exception is the western Nansen Basin, where the weaker halocline allows vertical ventilation of the AW up to the surface (Carmack et al., 2015; Koenig et al., 2017; Onarheim et al., 2014). However, the Arctic Ocean has undergone a substantial weakening of the stratification at the base of the mixed layer (Polyakov et al., 2017; Toole et al., 2010). Hence, conditions previously unique to the western Nansen Basin (weaker halocline, shallower AW layer) are now observed in the eastern Eurasian Basin as well (Polyakov et al., 2017). This northeastward progression of the western Eurasian Basin conditions (enhanced upward AW heat fluxes, diminished sea ice cover and volume) has been called

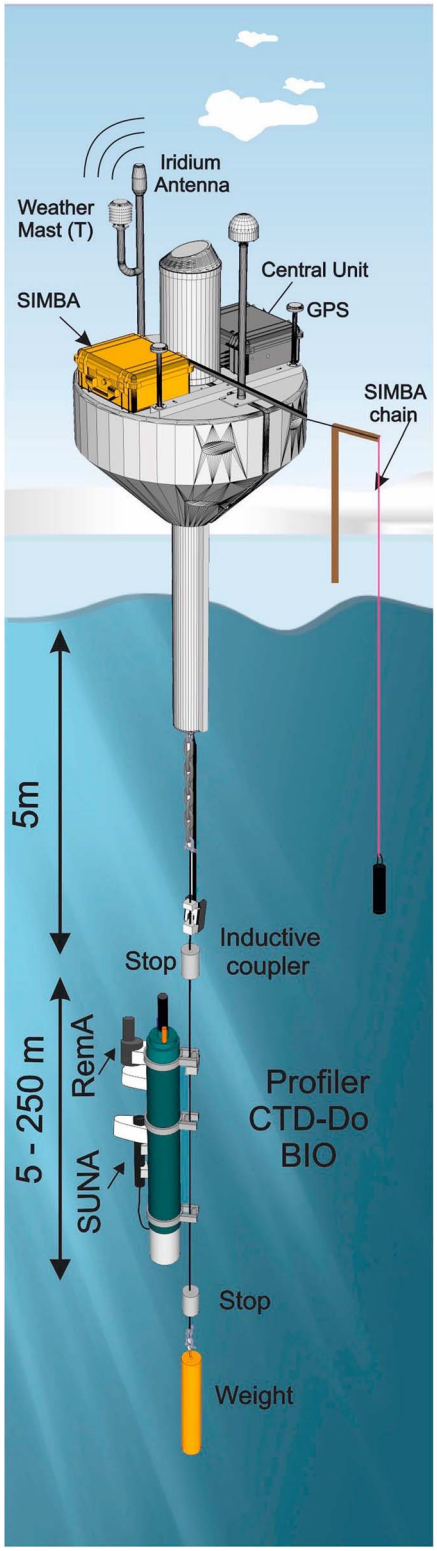

Figure 1. Schematic of IAOOS platform 24. The ocean profiler was equipped with bio-optics sensor suite (pack Rem-A) and a nitrate sensor (SUNA) in addition to the traditional CTD-DO sensors. SIMBA = Scottish Association for Marine Sciences ice mass balance for the Arctic; CTD = conductivity, temperature, and depth; SUNA = submersible ultraviolet nitrate analyzer.

"Atlantification" of the Arctic Ocean (Polyakov et al., 2017). The recent weakening of the halocline, combined with the shoaling of AW, is the main driver for these changes (Polyakov et al., 2017; Rabe et al., 2014). In this context of Atlantification, the role of AW in sea ice reduction in the Eurasian Basin is likely becoming increasingly important (Carmack et al., 2015; Polyakov et al., 2017).

Since 2004, autonomous drifting systems such as ice-tethered profilers (Krishfield et al., 2008) have helped to document water physical properties (temperature and salinity) across a vast portion of the Arctic Ocean's top 800 m. Recently, sensors have been added to profilers to document dissolved oxygen (DO) concentration (Timmermans et al., 2010) or upper ocean bio-optical properties (e.g., Laney et al., 2014). In parallel with observational efforts, performances of operational models in the Arctic have significantly improved in the past decade. For example, Mercator Ocean operational model outputs have been shown to compare fairly well with profiler data from autonomous drifting IAOOS (Ice Atmosphere Ocean Observing System) platforms north of Svalbard (Koenig et al., 2017) and helped put the observations in perspective.

Two IAOOS platforms (Figure 1) provided an 8-month-long data set in the Eurasian Basin in 2017. One of the ocean profilers was equipped with biogeochemical capabilities and in particular measured nitrate concentration and colored dissolved organic matter (CDOM). The ocean data acquired during the meandering IAOOS platform trajectories (Figure 2) uniquely document the physical and biogeochemical characteristics of the upper water column in the western Eurasian Basin (>790 profiles) in 2017.

The paper is organized as follows. Section 2 presents the IAOOS data, Mercator Ocean operational system, and WOA13 climatology. Section 3 describes the different hydrographic regions sampled by the profilers. Notable mesoscale structures in the halocline and in the warm AW layer are studied in section 4. The IAOOS 2017 data are compared to the 2005–2012 WOA13 climatology in section 5.1. In section 5.2, the Mercator Ocean model performance is evaluated against the 2017 IAOOS observations. The contribution of the model outputs to the analysis of the observed mesoscale structures is discussed in section 5.3. Results are summarized and discussed in section 6.

2. Data

2.1. IAOOS Ocean and Ice Data

The IAOOS autonomous platforms document the four media —ocean, ice, snow, and atmosphere— while drifting with the ice (Provost et al., 2015). The standard IAOOS platform carries a weather mast and a micro-lidar for the atmosphere (Mariage et al., 2017), an ice mass balance instrument (K. Jackson et al., 2013), and an ocean profiler (Koenig et al., 2016). Two platforms (IAOOS 23 and IAOOS 24) were deployed at the North Pole from the Russia-operated Barneo ice camp on 12 April 2017. The platforms have slightly different configurations, with one of them carrying additional biogeochemical sensors (Figure 1 and Table 1). Although we focus here on the physical parameters, we also examine selected biogeochemical parameters considered as water mass tracers to the first order, namely, DO concentration, nitrate concentration, and CDOM.

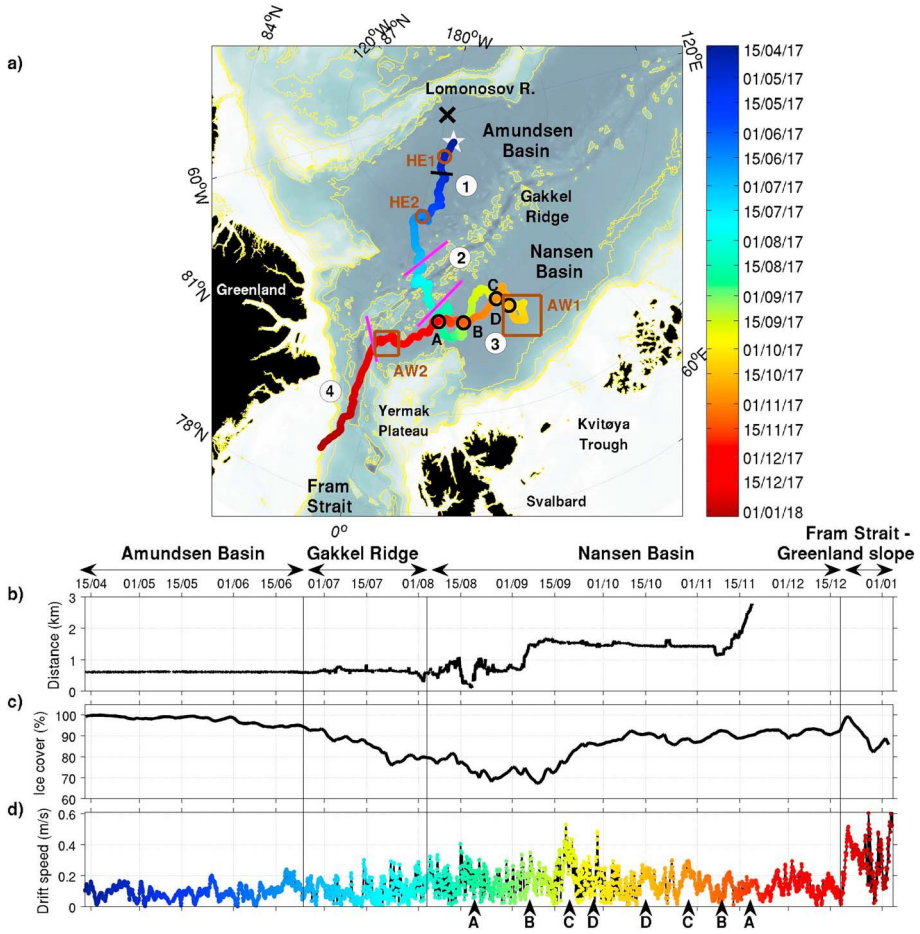

Figure 2. (a) Drift trajectory of the IAOOS platforms from 12 April 2017 to 4 January 2018. Color code is time, bathymetry (IBCAO) is in gray scale with yellow isolines at 0, 500, 700, 1,000, 2,000, and 3,200 m. Magenta lines delineate the four regions: (1) the Amundsen Basin, (2) the Gakkel Ridge, (3) the Nansen Basin, and (4) the western Fram Strait and Greenland continental slope. Black line at 88.2°N indicates a frontal zone. Black circles indicate the four crossover points (A, B, C, and D). Brown circles indicate the location of two halocline eddies (HE1 and HE2), and brown boxes the location of two Atlantic Water (AW) mesoscale structures (AW1 and AW2). The black cross marks the North Pole. (b) Time series of the distance between the two platforms. (c) Sea ice concentration (%) from Mercator Ocean operational model collocated with the drift. (d) Drift speed (m/s) of the platforms. Arrows on the top and vertical lines through panels (b) to (d) indicate the limits of the regions. Dates of the crossover points are indicated below panel (d).

The ocean profiler on IAOOS 24 was a PROVOR SPI (from French manufacturer NKE) equipped with a Seabird SBE41 conductivity, temperature, and depth and a DO Aandera 4330 optode. The profiler on IAOOS 23 carried additional biogeochemical sensors including a bio-optics sensor suite and a nitrate sensor (Figure 1). The bio-optics sensor suite (called Pack Rem-A) combines a three-optical-sensor instrument (ECO Triplet, WET Labs Inc.) and a multispectral radiometer (OCR-504, Satlantic Inc.). We use the CDOM fluorescence (excitation/emission 370/460 nm) from the WETLabs ECO sensor. The nitrate sensor was a submersible ultraviolet nitrate analyzer (SUNA, Satlantic-Seabird Inc.), a chemical-free ultraviolet nitrate sensor. The profilers were set to perform two upward profiles per day from 250 m (IAOOS 23) and 350 m (IAOOS 24) starting at approximately 6 a.m. and 6 p.m. UT. They provided a unique 8-month-long data set, by gathering a total of 793 profiles of the temperature, salinity, and oxygen (upper 350 m) and 427 profiles of CDOM and nitrate concentrations (upper 250 m; Table 1). No bottle observations were collected.

The conductivity, temperature, and depth data have a vertical resolution of 1 db. We use the International Thermodynamic Equations of Seawater (TEOS-10) framework (McDougall et al., 2012) with conservative temperature CT (°C) and absolute salinity (g/kg). In our study region, absolute salinity values exceed practical salinity values by about 0.16. After data quality control processing, 97% of IAOOS 23 and 95% of IAOOS

Table 1
Summary of IAOOS 23 and 24 Ocean Data: Sensors, Sampling Rates and Number of Profiles

Platform	Dates of acquisition			Wire length (m)	Acquisition duration (days)		Profiles performed			Profiles validated	
IAOOS 23	12 April 2017 – 4 January 2018			250	268		439 (82% of expected)			427 (97% of performed)	
IAOOS 24	12 April 2017 – 16 November 2017			350	219		387 (88% of expected)			366 (95% of performed)	
Equipment/sensor	SUNA	ECO triplet	ECO triplet	ECO triplet	OCR	OCR	CTD	CTD	CTD	CTD	DO optode
Parameters	[NO$^-$] (µM)	Chl a (µg/L)	CDOM (ppb)	BP (m^{-1})	PAR	Ed	T (°C)	S (g/kg)	Depth (dbar)	DO (µM)	
Accuracy	±2 µM	±0.025 µg/L	±0.28 ppb	±0.003 m	±0.01	±0.0025	±0.005°C	±0.02 g/kg	±2 dbar	±3 µM	
Vertical resolution	10 dbar	1 dbar	1 dbar	1 dbar	1 dbar	1 dbar	1 dbar	1 dbar	1 dbar	2 dbar	
IAOOS 23	Yes	Yes	Yes	Yes	Yes	Yes	Yes	Yes	Yes	Yes	
IAOOS 24	No	No	No	No	No	No	Yes	Yes	Yes	Yes	
Used (U)/Not Used (NU)	U	NU	U	NU	NU	NU	U	U	U	U	

Note. IAOOS = Ice Atmosphere Ocean Observing System; SUNA = submersible ultraviolet nitrate analyzer; CTD = conductivity, temperature and depth; DO = dissolved oxygen; CDOM = colored organic matter.

24 data were retained. The data from the two profilers were corrected independently from one another. We removed salinity spikes associated with sharp gradients within double-diffusive thermohaline staircases as in Dmitrenko et al. (2008). The two profilers' data sets showed great coherence and an offset of 0.01 g/kg in salinity, corrected by applying an offset +0.005 and −0.005 g/kg to data from profilers 23 and 24, respectively. The accuracy was estimated to be 0.005 °C in temperature and 0.02 g/kg in salinity.

The DO data have a 2-db vertical resolution. DO concentrations were retrieved following Thierry et al. (2016). Apparent oxygen utilization (AOU) was computed from the profilers' DO concentrations and compared to AOU derived from DO bottle measurements from the North Pole Environmental Observatory, years 2013 and 2014 (ftp://northpoleftp.apl.washington.edu/../NPEO_Data_Archive/NPEO_Chemistry/CTD-Oxygens/). The comparisons (not shown) suggested a systematic negative offset (about −26 µmol/kg for the IAOOS 24 optode at 250 m and −30 µmol/kg for the IAOOS 23 optode at 360 m), which was corrected. AOU values from the two profilers were consistent throughout the drift with a nearly constant difference of 2.5 µmol/kg at 250-m depth, while the values ranged from 20 to 60 µmol/kg. The nitrate concentration was computed from the observed spectrum (submersible ultraviolet nitrate analyzer) using the Temperature Compensated Salinity Subtracted algorithm developed by Sakamoto et al. (2009) following ARGO DAC protocol (Johnson et al., 2018). Nitrate concentrations were calibrated using 2014 NPEO bottle data and adjusting the optical wavelength offset to 212.5 nm (Johnson et al., 2018). The estimated accuracy of the nitrate observations is 2 µmol/kg (comparison with NPEO values and theoretical sensor accuracy), with a vertical resolution of 10 db. The CDOM fluorescence data are presented as reported by the ECO triplet converted from raw counts to the physical unit (ppb) but uncorrected for any offset beyond that determined during factory calibration. CDOM data have a 1-db vertical resolution, and a manufacturer accuracy of ±0.28 ppb.

The two platforms were initially located 600 m from each other. They drifted together following meandering trajectories, reaching as far as 30°E in the Nansen Basin in mid-October 2017, when they changed direction and drifted back toward Fram Strait (Figure 2a). The profiler IAOOS 24 stopped transmitting on 16 November 2017, the two platforms being separated by about 3 km at that time (Figure 2b). Profiler IAOOS 23 acquired data until 4 January 2018. The meandering drift paths led to four crossover points visited at different times (points A, B, C, and D in Figure 2). Differences between two measurements made some time apart at the same location can be due to either natural in situ variations or instrumental drift. The platforms visited location 83.79°N, 12.55°E (point A in Figure 3) within a 94-day interval (18 August and 20 November 2017). Temperature, salinity, DO, and CDOM were very consistent in the 150- to 250-m depth range indicating that there was no sizable instrumental drift throughout the 8-month-long data set. Interesting differences were observed in the upper 150 m: These are the consequence of seasonal variations and are examined in section 3.3. Nitrate concentrations show a constant difference of about 1.5 µmol/kg over the 150- to 250-m range between the two visits to point A. This offset is small compared to the range of the nitrate concentrations of IAOOS 23 (0 to 12.5 µmol/kg), which is the range of the relatively scarce observations in that part of the Arctic Ocean (e.g., Codispoti et al., 2013; Randelhoff & Guthrie, 2016).

Several profiles did not reach the near surface: a strong stratification in the halocline could have impeded the ascent of the profiler, particularly in July–August 2017 when sea ice melted (Figure 2c) to inject fresh water underneath the sea ice, resulting in a strong density gradient at about 30-m depth (Figure 4). Large drift velocities (>30 cm/s) encountered in the Nansen Basin (Figure 2d) also contributed to prevent the ascent of the profiler. Several profiles are missing late August and late September due to data logger issues (now resolved for future IAOOS deployments).

The two platforms were also equipped with a Scottish Association for Marine Sciences ice mass balance for the Arctic (SIMBA) system: a 5-m chain measuring temperature and a proxy of the

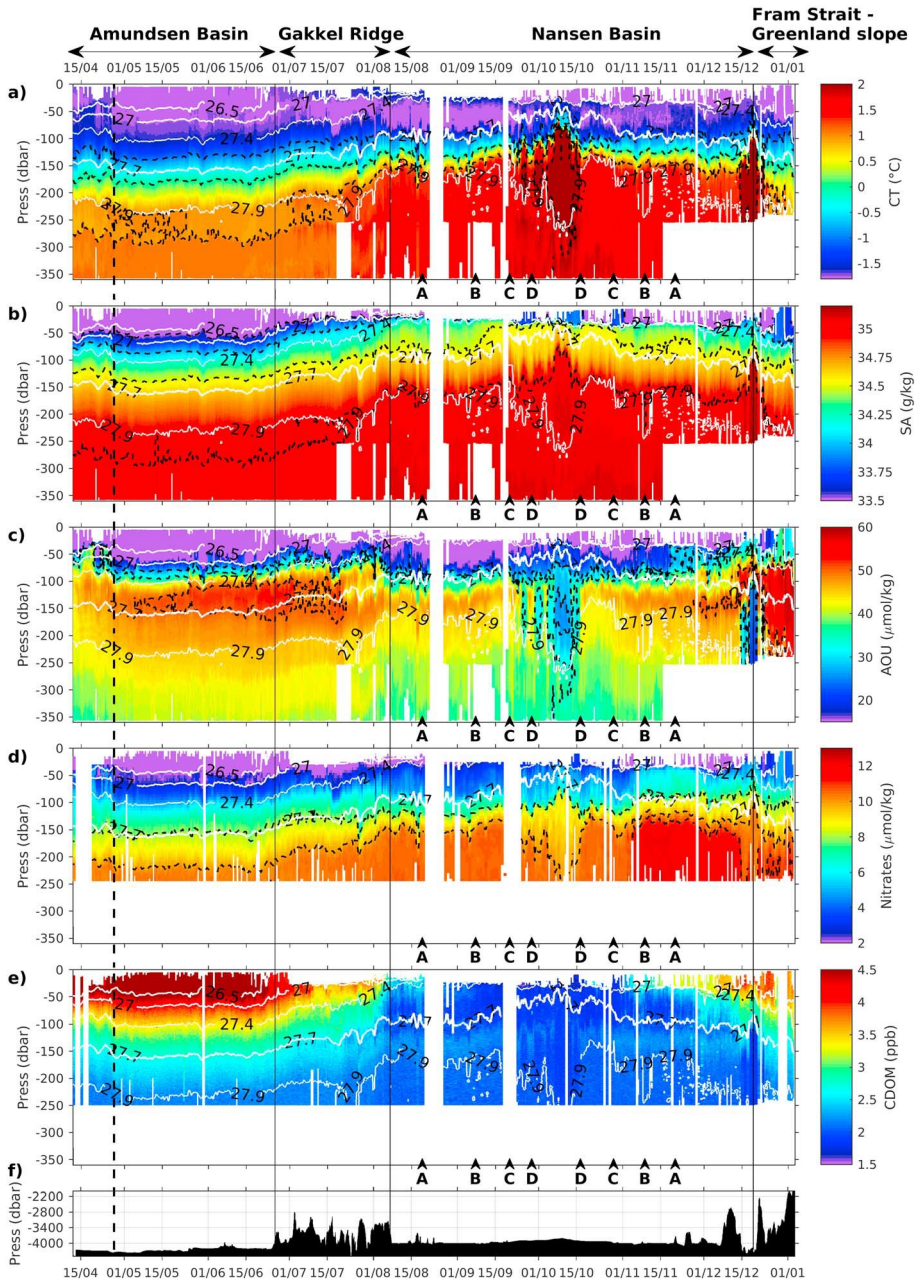

Figure 3. Composite sections from the two profilers: (a) conservative temperature (°C; the thick dashed black line marks the 0 °C isotherm), (b) absolute salinity (g/kg), and (c) apparent oxygen utilization (µmol/kg). Composites were obtained by averaging the data from the two profilers when available and keeping the available data otherwise. (d) Nitrate (µmol/kg) and (e) colored dissolved organic matter (ppb) from biogeochemical profiler IAOOS 23. (f) Bathymetry along the drift trajectory. Black dashed lines are, respectively, temperature, salinity, apparent oxygen utilization and nitrate isolines. White lines are isopycnals, and the thick one marks 27.7 kg/m^3. The four regions are labeled on top of panel (a) and their limits indicated with vertical lines through all panels. The dashed vertical line marks the 88.2°N latitude. Crossover points A, B, C, and D from Figure 2 are reported below the sections.

thermal resistivity of the media with a 2-cm vertical resolution (K. Jackson et al., 2013). The sampling frequency was set to 2 hr, and the sensor accuracy is 0.1 °C (Table 1). The SIMBA record on IAOOS 23 was short (not shown). The SIMBA on IAOOS 24 acquired data from 13 April to 12 November 2017. The tripod to which the chain was attached fell down on 30 July 2017, and the data in the upper part of the chain (air, snow and upper part of the sea ice) are not reliable after that date. The ocean-ice interface was

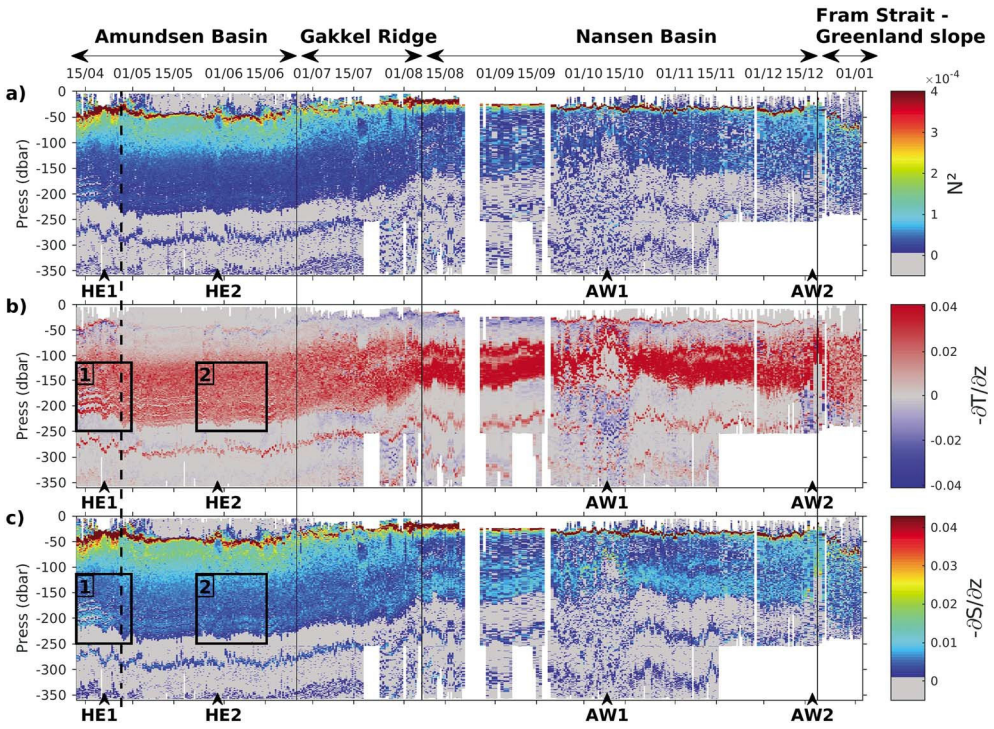

Figure 4. Sections of (a) Brunt-Väisälä frequency (N^2), (b) vertical gradient of conservative temperature $\partial T/\partial z$ (°C/m), and (c) vertical gradient of absolute salinity $\partial S/\partial z$ (g/kg/m) derived from the composite sections. The four regions are labeled on top of panel (a) and their limits indicated with vertical lines through all panels. The dashed vertical line marks the 88.2°N latitude. In (b) and (c), box 1 indicates the position of three steps in temperature and salinity at the base of the thermocline. South of 88.2°N, the steps are substantially eroded and hardly distinguishable in box 2.

estimated following the method described in Provost et al. (2017), based on the detection of changes in the vertical temperature gradient.

The information regarding the data acquired during platform drifts (resolution, sampling accuracy) is summarized in Table 1.

2.2. World Ocean Atlas Climatology

World Ocean Atlas 2013 version 2 (WOA13 V2; Locarnini et al., 2013; Zweng et al., 2013; https://www.nodc.noaa.gov/OC5/woa13/) is a long-term set of objectively analyzed climatologies of temperature, salinity, oxygen, phosphate, silicate, and nitrate available at annual, seasonal, and monthly resolution for the World Ocean. Here we use the WOA13 version 2 monthly averages over the most recent 2005–2012 period. The temperature and salinity fields have a (1/4)° horizontal resolution, with 102 vertical levels of resolution 1 m at the surface to 200 m at 5,500 m.

2.3. Mercator Ocean Operational System

The (1/12)° global Mercator Ocean operational system was developed for the Copernicus Marine Environment Monitoring Service (http://marine.copernicus.eu/), with a (1/12)° horizontal resolution and 50 vertical z levels. The modeling component is based on the NEMO (Nucleus for European Modeling of the Ocean; Madec, 2008) platform and the assimilation system is a multidata and multivariate reduced order Kalman filter based on the singular extended evolutive Kalman filter formulation introduced by Pham et al. (1998). The model uses the LIM2 thermodynamic sea ice model and is driven at the surface by atmospheric analysis and forecasts from the Integrated Forecasting System operational system at European Centre for Medium-Range Weather Forecasts. The assimilated observations are along-track satellite altimetry, sea surface temperature (OSTIA SST), and in situ vertical profiles of temperature and salinity. The system PSY4V3 assimilates OSI SAF (http://cmems-resources.cls.fr/documents/QUID/CMEMS-OSI-QUID-011-001to007-009to012.pdf) sea ice concentration in both hemispheres with a monodata and monovariate scheme. A particular treatment is applied for areas potentially covered in sea ice: The observation error in the multivariate

singular extended evolutive Kalman filter increases linearly (less weight in the analysis) with the decrease of the SST from −1 to −1.7 °C, and the observation is rejected if SST is less than −1.7 °C (i.e., an approximation of the freezing point). In other words, apart from the sea ice concentration no quantities are assimilated in ice covered oceans. A monthly runoff climatology based on coastal runoffs and 100 major rivers from the Dai et al. (2009) database is used. A full description of the system components is available in Lellouche et al. (2018). The system starts in October 2006 from a "cold" start (initial currents are null) and from EN4.2.1 hydrographic temperature and salinity data (Good et al., 2013).

3. Hydrography of the Western Eurasian Basin in April 2017 to January 2018

We define water mass boundaries following Rudels et al. (2000); see Figure 5g. In the Eurasian Basin, the upper layer mainly comprises Polar Surface Water (PoSW, density σ_θ<27.7 kg/m^3). The mixed layer depth is estimated to be at the point of maximum buoyancy frequency N^2, that is, depth of maximum stratification. The stratification at the bottom of the mixed layer evolves geographically and seasonally. The thermocline is predominantly found below the halocline (Figures 5a and 5b), with differences in depth of up to 75 m. The warm layer typically extends between about 150 and 500 m and comprises two main water types: Atlantic Water (AW, $T > 2$ °C) and Modified Atlantic Water (MAW, $T < 2$ °C). Both warm water types occupy the same potential density range of 27.7–28.0 kg/m^3 (Rudels et al., 2000; Schauer et al., 2002; AW and MAW in Figure 5g). In the present data set, the lowest apparent oxygen utilization (AOU ~ −10 to +20 μmol/kg) is located near the surface (Figure 3c). A thin layer of maximum oxygen utilization (AOU ~ 50 μmol/kg) is observed near 120-m depth. Nitrate concentrations monotonically increase with depth, from $[NO_3^-]$ ~ 1–4 μmol/kg near the surface up to a maximum of $[NO_3^-]_{max}$ ~ 12 μmol/kg at 250 m (Figure 3d).

During their drift, the IAOOS platforms crossed several hydrographic regions with distinct characteristics (delineated by the magenta lines in Figure 2a): the Amundsen Basin from 12 April to 25 June (region 1 in Figure 2a), the Gakkel Ridge from 26 June to 5 August (region 2), the Nansen Basin from 6 August until 19 December (region 3), and the western Fram Strait-Greenland slope from 20 December until the end of the acquisition on 4 January 2018 (region 4).

Each region is described in the following subsections and the main characteristics are summarized in Table 2.

3.1. Amundsen Basin: 12 April to 25 June 2017 (152 Profiles)

Two hydrographic regions subdivide the Amundsen Basin. North of 88.2°N (vertical dashed line in Figures 3, 4, and 6), surface salinities lower than 32.5 g/kg were observed in the 30-m-deep mixed layer, with temperatures close to the associated warmer freezing point (S ~ 32.18 g/kg, T ~ −1.7 °C, Figures 6a and 6c). Below the mixed layer, waters are warmer, saltier, and denser and have larger AOU and nitrate concentrations than in the rest of the Amundsen Basin (Figures 3 and 6). South of 88.2°N, the mixed layer exhibits slightly larger salinities and temperatures close to the cooler freezing point (S ~ 32.86 g/kg, T ~ −1.77 °C). This frontal region results from the confluence of fresher water from the Makarov Basin (Timmermans et al., 2011) and Eurasian water, north and south, respectively, of 88.2°N (Figures 3 and 6).

During the platforms' drift through the entire Amundsen Basin, the ice thickness increased (growth ~ 10 cm, Figure 6a). A notable CDOM maximum in the upper 100 m ([CDOM] > 3 ppb) was associated with a minimum in nitrate ($[NO_3^-]$ ~ 0–4 μmol/kg; green curves in Figures 5; Figures 6d and 6e) and overlays a thick zone of maximum oxygen utilization (AOU ~ 45 μmol/kg between 100- and 200-m depths; Figures 5d and 6d). This is the vestige of past biological activity in the water mass. This water is likely a mixture of shelf water and fresh Siberian river runoff that is carried by the Transpolar Drift (TPD) across the central Arctic Basin to reach the Amundsen Basin (Figure 6c; Damm et al., 2018; Kipp et al., 2018).

The thermocline extended between 80 and 220 m ($|\partial_z T|$ ~ 0.02 °C/m; Figures 4b and 5a), while the halocline is between 30 and 220 m deep with a relatively moderate salinity gradient ($|\partial_z S|$ ~ 7 ×10^{-3} g/kg/m; Figures 4c and 5b). In the Makarov-origin water north of 88.2°N, three homogeneous layers of temperature and salinity and very weak stratification (hereafter called "steps") are visible at the base of the thermocline (characterized by N^2~0, $|\partial_z T|$ ~ 0 °C/m and $|\partial_z S|$ ~ 0 g/kg/m, box 1 in Figures 4b and 4c). The steps are located at roughly 165-, 180-, and 200-m depths and have a vertical extent of ~10 m. South of 88.2°N, the steps are substantially eroded in temperature and are no longer visible in salinity (box 2 in Figures 4c and 4d).

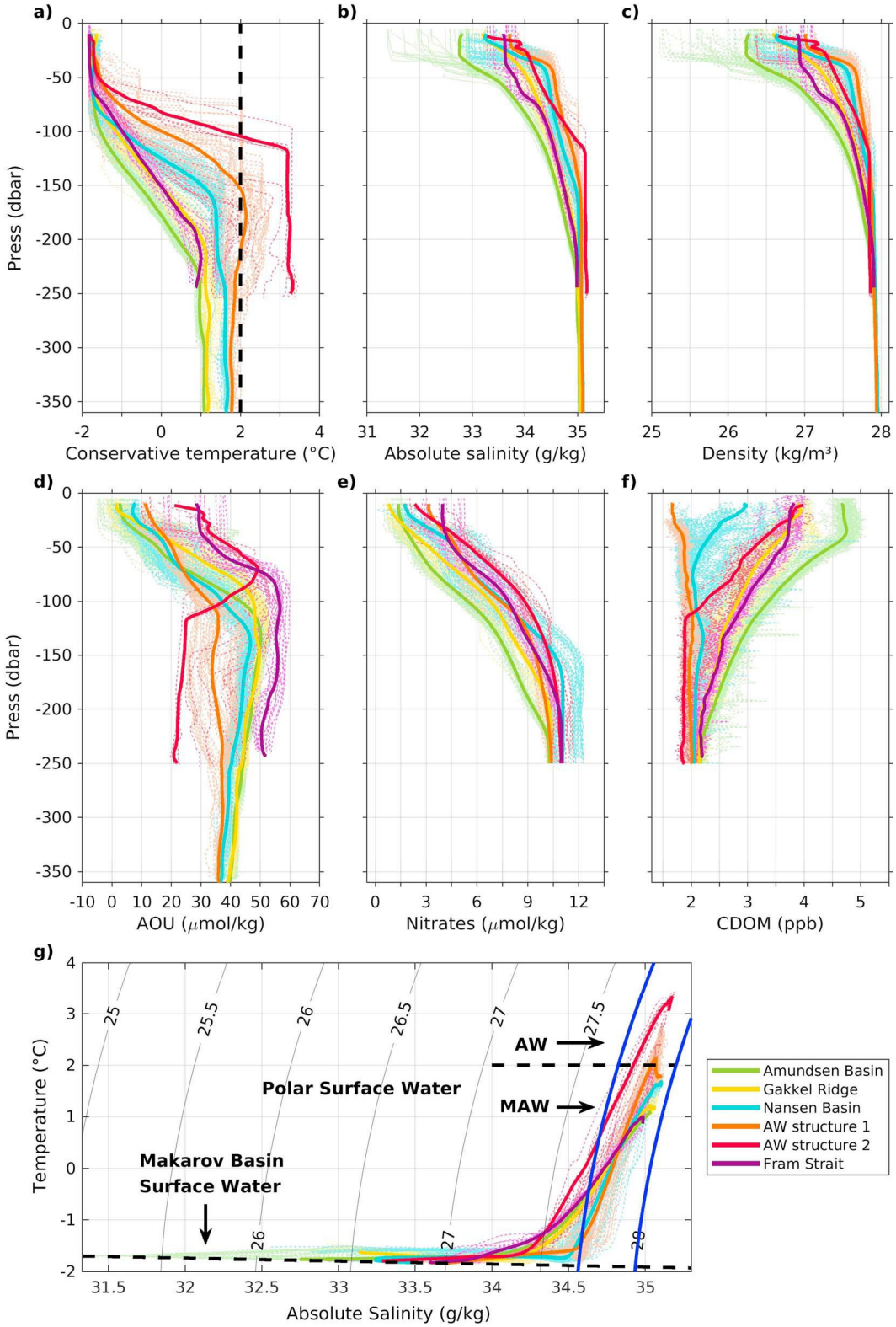

Figure 5. Vertical profiles of (a) conservative temperature (°C), (b) absolute salinity (g/kg), (c) density anomaly (kg/m^3), and (d) apparent oxygen utilization (μmol/kg) from the two profilers. (e) Nitrate (μmol/kg) and (f) CDOM (ppb) from IAOOS 23. (g) TS diagram. Colors correspond to the different regions: the Amundsen Basin in green, the Gakkel Ridge in yellow, the Nansen Basin in blue, AW structure 1 in orange, AW structure 2 in red, and the Fram Strait in purple. Dashed lines are daily profiles; thick lines average profiles in each region. In (a) and (g), the thick black dashed line indicates the 2 °C temperature limit distinguishing MAW (<2 °C) and AW (>2 °C). CDOM = colored dissolved organic matter; AW = Atlantic Water.

Table 2
Hydrographic Characteristics of the Four Regions

		Amundsen Basin				
		North of 88.2°N	South of 88.2°N	Gakkel Ridge	Nansen Basin	Fram Strait - Greenland slope
Dates		12 April 26 April	26 April 25 June	25 June 5 August	5 August 19 December	19 December 4 January
STM or NSTM		No	No	Yes	Yes	No
Mixed layer[a]	Depth (m)[a]	22 ± 10	36 ± 9	Tilted isolines	30 ± 6	40 ± 6
	CT (°C)[a]	−1.70 ± 0.02	−1.77 ± 0.01		−1.76 ± 0.01	−1.80 ± 0.01
	$\overline{SA}$ (g/kg)[a]	32.18 ± 0.20	32.86 ± 0.04		33.74 ± 0.12	33.62 ± 0.02
	[CDOM] (ppb)[a]	4.70 ± 0.28	4.71 ±0.28		2.83 ± 0.28	3.73 ± 0.28
50 m	$\overline{CT}$ (°C)	−1.65 ± 0.02	−1.77 ± 0.01	Tilted isolines	−1.69 ± 0.03	−1.75 ± 0.03
	$\overline{SA}$ (g/kg)	33.42 ± 0.08	33.40 ± 0.05		34.43 ± 0.02	33.85 ± 0.09
	$\overline{AOU}$ (µmol/kg)	28.66 ± 10.91	12.35 ± 3.70		20.23 ± 6.96	33.77 ± 4.46
	$\overline{NO_3^-}$ (µmol/kg)	3.63 ± 2.00	2.34 ±2.00		4.82 ± 2.00	4.59 ± 2.00
	$\overline{[CDOM]}$ (ppb)	4.33 ± 0.28	4.50 ±0.28		2.19 ± 0.28	3.54 ± 0.28
MAW layer	Depth (m)	144 ± 4	158 ± 4	Tilted isolines	86 ± 23	128 ± 16
	$\overline{CT}$ (°C) top core	0.92 ± 0.01		1.12 ± 0.01	1.40 ± 0.04	0.98 ± 0.03
	$\overline{CT}$ (°C) lower core	1.08 ± 0.01		1.15 ± 0.02	1.61 ± 0.02	NA
	$\overline{SA}$ (g/kg) top core	34.99 ± 0.02		35.00 ± 0.02	35.03 ± 0.02	34.98 ± 0.02
	$\overline{SA}$ (g/kg) lower core	35.03 ± 0.02		35.04 ± 0.02	35.07 ± 0.02	NA
	$\overline{AOU}$ (µmol/kg)	45.23 ± 0.06		45.12 ± 0.49	42.72 ± 0.60	53.00 ± 0.63
	$\overline{NO_3^-}$ (µmol/kg)	9.32 ± 2.00		10.03 ± 2.00	10.27 ± 2.00	10.34 ± 2.00
	$\overline{[CDOM]}$ (ppb)	2.34 ± 0.28		2.34 ± 0.28	2.11 ± 0.28	2.28 ± 0.28

Note. For each parameter, region-averaged value is accompanied with its corresponding standard deviation. The mixed layer depth is estimated with a 0.03 kg/m^3 density difference with the surface values. Several profiles are missing above 20m whereas the 50 m level is well documented. Hence, CT, SA, AOU, NO_3^- and [CDOM] at 50 m provide a robust characterization of the near-surface regional variations. The MAW layer depth corresponds to the depth of the 27.7 kg/m^3 isopycnal. NSTM = near surface temperature maximum; CDOM = colored dissolved organic matter; AOU = apparent oxygen utilization; MAW = Modified Atlantic Water; NA = not available.
[a]Subject to caution as several profiles do not reach the surface (< 20 m deep).

In the Amundsen Basin, the warm layer is shallower north of the frontal zone (~140 m) than south (~160 m) and is composed of MAW. Figure 4 shows two distinct, thick MAW layers of homogeneous temperature and salinity (N^2~0). The top layer is slightly thinner than the lower layer (respectively, ~50 and 70 m). They are separated by a thin, sharp interface of positive of N^2 corresponding to steep vertical temperature and salinity gradients of 0.035 °C/m and 0.005 g/kg/m (Figures 4b and 4c). This interface is located at 270 m north of 88.2°N and 290 m south (in temperature, salinity, and N^2). For the top and lower layers, temperatures are around 0.92 and 1.08 °C, and salinities are about 34.99 and 35.03 g/kg (Figures 3 and 5).

Two cold core anticyclonic halocline eddies were detected (core depth ~50 m) near 87°N, 5°E and 89°N, 8°E, at a time when the drift trajectory was straight (indicated as HE1 and HE2 in Figures 2, 4, and 6) using the method described in Zhao et al. (2014) based on isopycnal displacements. The two eddies have characteristics typical of surface water: salinity similar to the environment (S ~ 33.75 g/kg), colder temperature (ΔT ~ 0.15 °C), oxygen-enriched (ΔAOU ~ −25 µmol/kg), and nitrate depleted (ΔNO_3^- ~ −1.5 µmol/kg). Due to the limitations of the eddy detection method, which requires at least four profiles in a relatively straight line (Zhao et al., 2014), several eddy-like isopycnal displacements during a sinuous trajectory were disregarded.

3.2. Gakkel Ridge: 26 June to 5 August 2017 (78 Profiles)

The Gakkel Ridge hydrographic region marks the transition between the Amundsen and Nansen basins, with tilted isolines corresponding to a shoaling of the warm MAW layer (Figure 3, yellow curves in Figure 5). CDOM sharply decreases and salinity increases (respectively, from 4.7 to 2.8 ppb and from

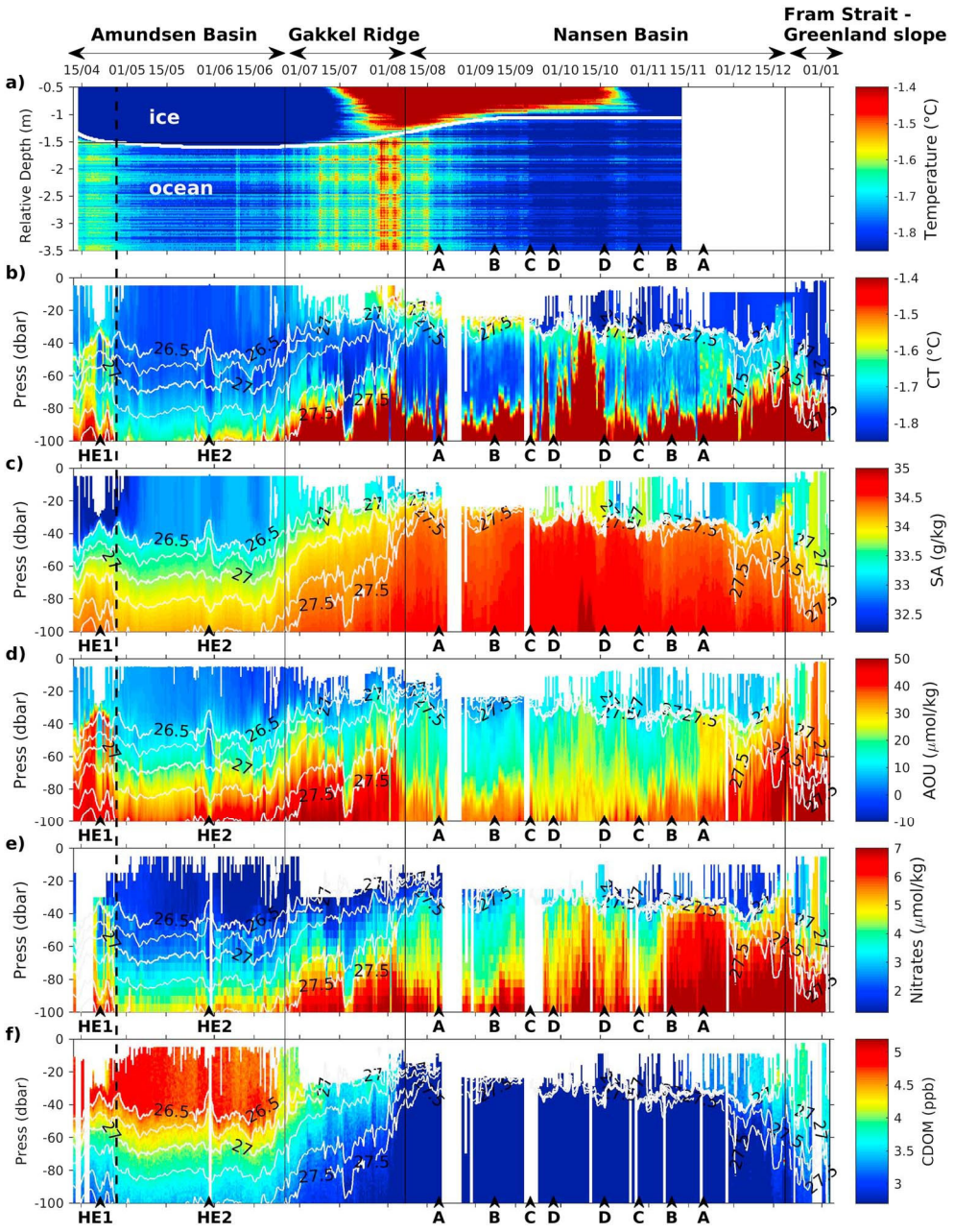

Figure 6. (a) Temperature in the ice and upper 2 m of the ocean from SIMBA chain. The white line delineates the ice-ocean interface. Composite sections in the upper 100 m of (b) conservative temperature (°C), (c) absolute salinity (g/kg), and (d) apparent oxygen utilization (AOU; μmol/kg). (e) Nitrate (μmol/kg) and (f) CDOM (ppb) from profiler 23 in the upper 100 m. Thin white lines are isopycnals. The four regions are indicated as in Figure 3. Halocline eddies (HE1 and HE2) and crossover points A, B, C and D are reported below the sections. The dashed vertical line marks the 88.2°N latitude, the southern limit of surface water fresher than 32.5. SIMBA = Scottish Association for Marine Sciences ice mass balance for the Arctic; CDOM = colored dissolved organic matter.

32.85 to 33.35 g/kg on average at 30-m depth; Figures 3 and 5). From late June to early August 2017, sea ice cover and thickness decrease by 15% and 25 cm, respectively (Figure 2c and 6a), the upper ocean warms by solar radiation and a surface temperature maximum is formed (Figures 6a and 6b; $\partial T/\partial z < 0$ at the surface in Figure 4b). The maximum surface temperature is reached in early August 2017 ($T \sim -1.45$ °C). Above the Gakkel Ridge, the homogeneous MAW layers sharply shoal from below 220 m in the Amundsen Basin to 150 m depth in the Nansen Basin (Figure 4).

Significant eddy-like isopycnal displacements are observed in the halocline, often associated with anomalies in temperature, AOU and nitrate (such as the anomaly observed around 17 July 2017 in Figure 6). However, the complex trajectory during this period prevents an interpretation in terms of halocline eddies. Isopycnals depths show a notable variability at the profile sampling rate (12 hr), probably indicative of topographically induced motions intensified above the Gakkel Ridge (Figure 4). The internal wave field in the Arctic, whether due to surface generated near-inertial waves or topographically induced internal tides (evanescent north of the critical latitude 74.5°N), has frequencies falling within the near-inertial frequency band (Dosser et al., 2014). The IAOOS platforms, set to perform profiles on a 12-hr frequency, only provide an estimate of the minimum internal wave amplitude of ~2 m above the Gakkel Ridge, in the Nansen Basin, and in the Fram Strait (Appendix A).

3.3. Nansen Basin: 6 August to 19 December (188 Profiles)

In the Nansen Basin, the platforms' meandering trajectory extensively documents the 83–85°N, 5–30°E area, except in the upper 20 m (Figure 3).

Near-surface salinities are in the range 32.8–33.8 g/kg (Figures 3 and 6, blue curves in Figure 5). Sea ice thickness decreases until mid-September and stabilizes around 1 m (Figure 6a). Sea ice melt, combined with the shoaling of the warm layer at ~80 m, induces a strong vertical salinity (and density) gradient between 20- and 40-m depths: the summer halocline ($|\partial_z S| \sim 6 \times 10^{-2}$ g/kg/m, Figures 4c and 5b; J. M. Jackson et al., 2010). The previously formed surface temperature maximum is progressively capped by cold and lighter water, leading to a near-surface temperature maximum (NSTM, Figure 6b). The NSTM located at 30-m depth by late September progressively mixes with the surrounding water (first passage at points C and D, Figure 6b). A thin layer of remnant NSTM persists as the platforms exit the Eurasian Basin in December 2017 (Figure 6b). The "lower halocline" is located between 40- and 160-m depth, with a significantly smaller vertical salinity gradient ($|\partial_z S| \sim 5 \times 10^{-3}$ g/kg/m, Figures 4c and 5b).

The thermocline is shallower and sharper than in the Amundsen Basin, between 70 and 150 m ($|\partial_z T| \sim 0.04$ °C/m, Figures 4b and 5a). The warm layer, mostly MAW, is located below 90-m depth, ~50 m closer to the surface than in the Amundsen Basin, and is nitrate enriched ($[NO_3^-] \sim$ 9–12 μmol/kg). Along with the top of the warm layer, the two layers of MAW shoal below 150 m and thicken. They are separated by an interface at ~230 m (Figures 4 and 5). The MAW layers exhibit warmer temperatures (respectively, ~1.4 and 1.6 °C) and larger salinities (respectively, 35.03 and 35.07 g/kg) than observed in the Amundsen Basin (Figures 3 and 5).

CDOM concentrations in the Nansen Basin are particularly low ([CDOM] ~ 2.1 ppb) and mostly homogeneous in the upper 250 m (Figures 3 and 5). However, at the level of the lower halocline (~130-m depth) a local CDOM maximum is observed ([CDOM] ~ 2.4 ppb) and matches the thin layer of maximum oxygen utilization (AOU ~ 50 μmol/kg, Figures 3c, 3e, 5d, and 5f), possibly indicating an active remineralization.

Two remarkable AW mesoscale structures are encountered in the Nansen Basin (Figures 2a and 3). The first structure, called hereafter AW1, was encountered near 83.5°N, 35°E between 24 September and 18 October 2017. The second structure, called hereafter AW2, was crossed north of the Yermak Plateau, near 82.8°N, 3°W between 14 and 20 December 2017. Both structures exhibited cores with temperatures larger than 2 °C, densities in the range 27.7–28 kg/m^3 and salinities larger than the surrounding MAW of the Nansen Basin ($\Delta S \sim +0.15$ g/kg): These core properties correspond to AW (Figure 5g). The two structures, examined in section 4.2, show significantly lower oxygen utilization than their environment as well as slightly lower nitrate concentrations (ΔAOU ~ 15–25 μmol/kg, $\Delta NO_3^- \sim -1$ μmol/kg).

3.4. Fram Strait-Greenland Slope: 20 December to 4 January (19 Profiles)

Platform 23 reached 83°N, 1°W on 19 December and exited the Eurasian Basin through the western Fram Strait. The profiler was lost on the Greenland continental shelf.

The near surface shows salinity around 33.3–33.8 kg/m^3 (purple curves in Figure 5; Figure 6) and a local CDOM maximum ([CDOM] ~ 3.5 ppb) associated with a surface nitrate maximum ($[NO_3^-] \sim$ 4.5 μmol/kg; Figures 5 and 6). Oxygen use is the highest recorded across the four regions (AOU ~ 50–60 μmol/kg). The variety of profiles corresponds to a frontal zone between the southward fresh and cold East Greenland Current and the salty and warmer AW recirculation branches (Sutherland & Pickart, 2008). In the

western Fram Strait, the warm layer, located below 130-m depth, is composed of cooler (~0.98 °C) and fresher (~34.98 g/kg) MAW exiting the Arctic Ocean (Sutherland & Pickart, 2008; Figures 3 and 5).

The next section focuses on the mesoscale structures crossed during the drift in the halocline near the North Pole and in the warm layer in the southwestern Nansen Basin.

4. Mesoscale Structures in the Western Eurasian Basin

4.1. Halocline Eddies

Two mesoscale structures located in the halocline were crossed at 89°N, 8°E and 87°N, 5°E in the Amundsen Basin (HE1 and HE2 in Figures 2, 4, and 6). They were identified as anticyclonic halocline eddies following Zhao et al. (2014). For halocline eddies 1 and 2, respectively (HE1 and HE2), six and nine consecutive profiles from each profiler showed anomalous convex isopycnal displacements while the drift trajectory was fairly straight (Figure 7). Assuming that both halocline eddies were crossed in their center, they have radii R_{HE} ~ 12 km, which is of the order of the Rossby deformation radius R_d in the region (in the Eurasian Basin R_d ~ 8 km, in the Canada Basin R_d ~ 13 km; Zhao et al., 2014; Figures 7a and 7b). Baroclinic velocities derived from density provide horizontal velocity difference between the eddy boundary and the center of about 5 and 3.5 cm/s for HE1 and HE2, respectively (Figures 7c and 7d). The eddy core depths are considered to be at the depth of the minimum temperature within the eddy (red markers in Figures 7e and 7f). The thickness of the eddy is defined by the distance between local maxima of the Brunt-Väisälä frequency N^2 above and below the eddy core (blue markers in Figures 7e and 7f). As HE1 does not have a maximum in N^2 below its core, its lower edge is roughly estimated from the temperature anomaly (cyan markers in Figure 7e). Both halocline eddies have core depths and thicknesses on the same order, with HE1 being slightly shallower and thicker (core depth ~ 45 and 55 m thick) than HE2 (core depth ~ 55 and 40 m thick). Maximum azimuthal baroclinic velocities are roughly at the same depth as the property cores (Figures 7c and 7d). Associated isopycnal displacements are visible as deep as 280 m for HE1 and possibly below (Figure 3) and extend down to 220 m for HE2 (Figure 4).

HE1 and HE2 are located, respectively, north and south of the frontal zone of Makarov-origin water at 88.2°N: Hence, the characteristics of their surrounding waters are rather different (as described in section 3.1). However, the two cores carry similar PoSW properties, with temperatures significantly colder than their environment (ΔT_{HE1} ~ −0.2 °C, ΔT_{HE2} ~ −0.08 °C), oxygen-enriched (ΔAOU_{HE1} ~ −30 µmol/kg, ΔAOU_{HE2} ~ −15 µmol/kg), and nitrate-depleted (ΔNO_3^-HE1 ~ −2 µmol/kg, ΔNO_3^-HE2 ~ −1 µmol/kg). The CDOM concentration in the cores is also somewhat lower ($\Delta CDOM_{HE1}$ ~ −0.4 ppb, $\Delta CDOM_{HE2}$ ~ −0.5 ppb) at the upper edge of the property cores. This suggests that the two halocline eddies were formed from the same surface water mass, despite their present location in different water masses. Possible sources of generation of these eddies are discussed in section 5.3.

4.2. AW Mesoscale Structures

Two AW mesoscale structures were crossed in the Nansen Basin (Figure 2a). The first AW structure (AW1) was encountered north of Kvitøya Trough (83.5°N, 35°E) as the platforms followed a hairpin turn (Figure 8a). AW1 is documented with 40 profiles over 22 days (40 from each profiler) from 25 September to 17 October 2017. The AW structure north of the Yermak Plateau (82.8°N, 3°W; AW2) was crossed in a straight line from 14 to 20 December 2017 (14 profiles in 7 days over 55 km and down to 250 m).

The AW mesoscale structures exhibit larger temperature and salinity than the surrounding MAW at about 1.5 °C and 35.05 g/kg in the Nansen Basin (Table 2). Their T-S characteristics are consistent with AW (orange curves for AW1 and red curves for AW2 in Figure 5). They are oxygen enriched compared to their environment (AOU_{env} ~ 45 µmol/kg). The core of AW2 is warmer (3 to 3.5 °C), saltier (35.2 g/kg), and more oxygen enriched (AOU_{AW2} ~ 20 µmol/kg) than the AW1 core (2.5 °C, 35.1 g/kg, AOU_{AW1} ~ 30 µmol/kg), which is likely explained by its greater proximity to the original inflow of AW through the Fram Strait (Figures 2a and 3). Both AW structures are nitrate-enriched compared to the surrounding PoSW at their upper boundary (ΔNO_3^- ~ +1.5 µmol/kg) although they are nitrate-depleted compared to the MAW layer (ΔNO_3^- ~ −1 µmol/kg).

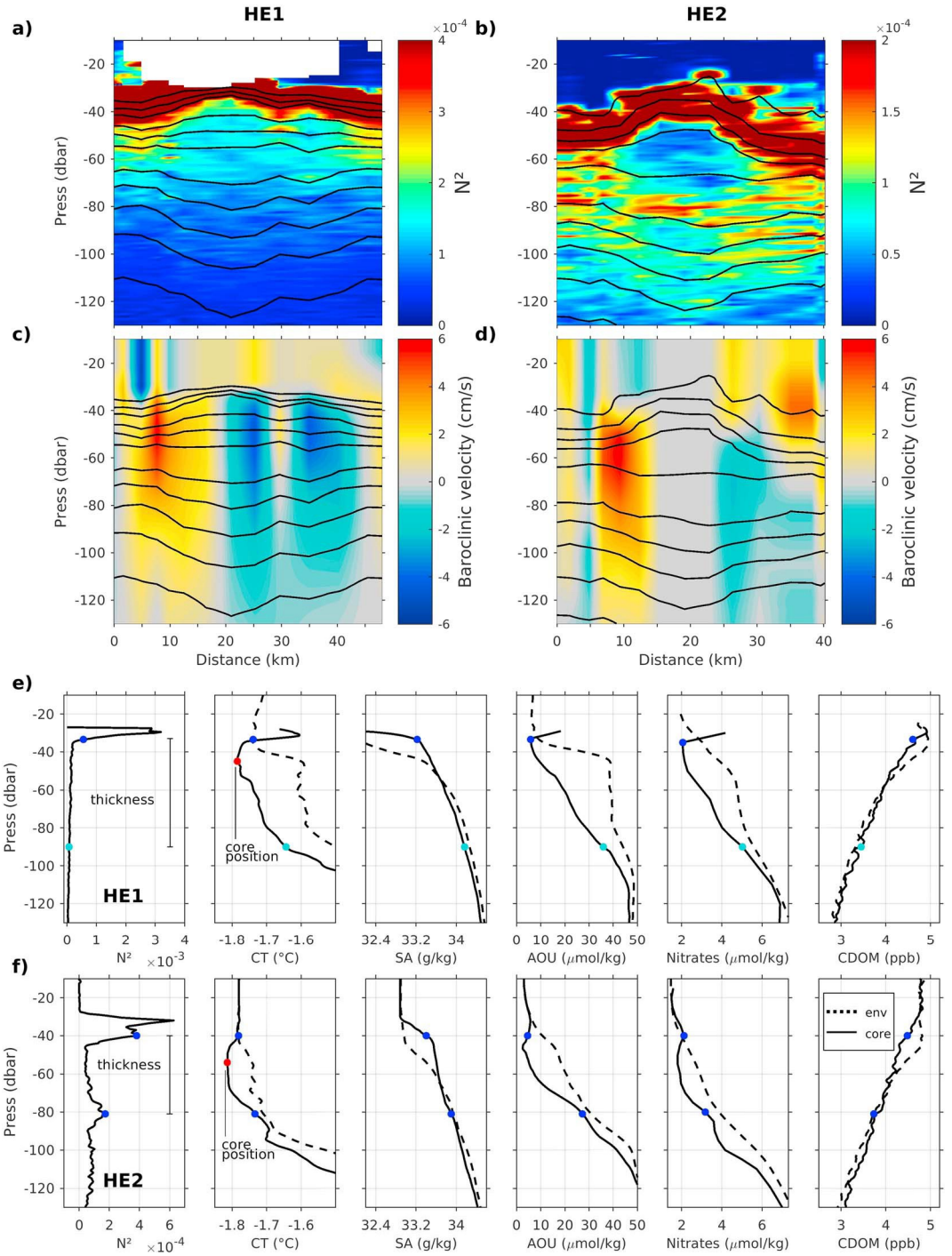

Figure 7. (a, b) Brunt-Väisälä frequency (N^2) in halocline eddies HE1 (crossed at 87°N, 5°E late April) and HE2 (crossed at 89°N, 8°E late May), respectively. (c, d) Baroclinic velocities (cm/s) in HE1 and HE2, respectively. Black lines are isopycnals. (e, f) Vertical profiles of N^2, conservative temperature (°C), absolute salinity (g/kg), AOU (μmol/kg), nitrate (μmol/kg) and CDOM (ppb) in the eddies core HE1 and HE2, respectively (solid black profiles). Dashed black profiles are from the eddy environment. AOU = apparent oxygen utilization; CDOM = colored dissolved organic matter; SA = salinity.

Both AW cores (depth of maximum temperature) are located around 180 m (Figures 3 and 5). AW1's thickness is about 190 m, with top and bottom edges at respectively 80 and 270 m (limits of the 2 °C criterion). AW2's top edge is located at 100 m; its thickness cannot be estimated (not documented below 250 m). A

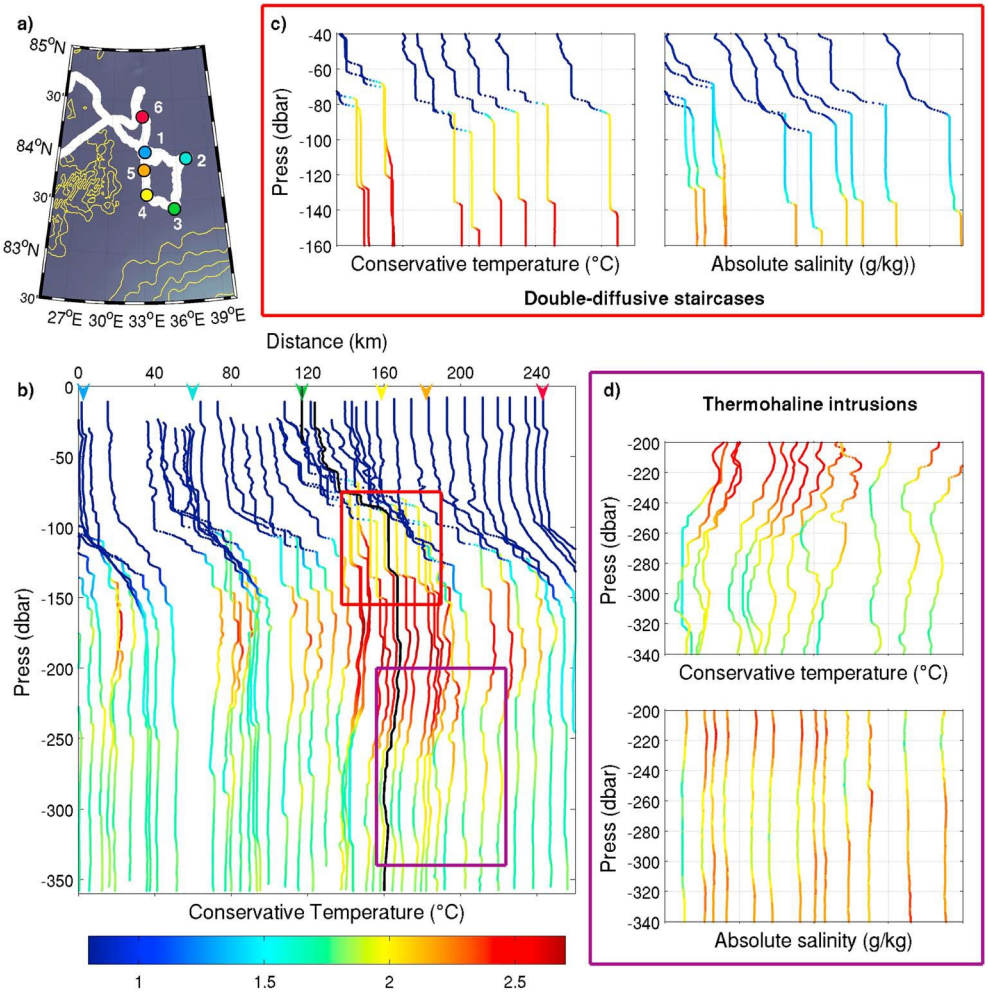

Figure 8. (a) Close-up on the platform trajectory when crossing mesoscale feature AW1 (white line). Yellow lines are bathymetry contours (−3,200, −2,000, −1,000, −500, and 0 m). Locations 1 to 6, in chronological order, are reported in (b). (b) Sequence of conservative temperature (°C) profiles from profiler IAOOS 24 from 24 September to 18 October within AW1. Each profile is offset from the previous one proportionally to the profile distance. Color code indicates conservative temperature. The black profile indicates the profile after which the platform backtracked. Double diffusive staircases are observed on the upper part of AW1 (red box), and intrusions are observed at the bottom edge of AW1 (purple box). The thick black profile indicates the southernmost location (labeled 3 in panel a). (c) Close-up on the red box: staircase-like features (double diffusive interfaces) in temperature and salinity. (d) Close-up on the purple box: inversions in temperature and salinity, consistent across several profiles, indicate thermohaline intrusions.

close examination of the temperature and salinity vertical profiles reveals intrusions and staircase structures, likely generated by double-diffusive processes (Figure 8). Several studies (e. g. Bebieva & Timmermans, 2016; Dmitrenko et al., 2008; Polyakov et al., 2018) used parameters such as the vertical density ratio to provide a quantitative characterization of the double-diffusive modes and to differentiate double-diffusive steps and intrusions. However, as the vertical resolution of the data set is around 1 dbar, we only provide a qualitative assessment of the vertical structure and double-diffusive features observed.

The "staircase structure" in AW1 indicates the presence of double-diffusive steps about 10 to 20 m thick at the upper limit of the structure in the thermocline (orange curves in Figure 5; Figures 8b and 8c). Thermohaline intrusions are observed above, on the sides of, and below AW1 (Figure 8d). In the upper part of AW1 (80 to 180 m), particularly thick (50 m) double-diffusive staircases are observed, separated by sharp, thin interfaces of strong vertical gradient in temperature (about 0.1 °C/m) and salinity (about 0.005 g/kg/m; Figures 4b and 8b). In the lower part of AW1 (180 to 270 m), vertically alternating intrusions and double-

diffusive staircases are observed (Figure 8), corresponding to successive positive and negative values of $\partial T/\partial z$ (Figure 4b).

AW2 exhibits somewhat different features with thicker steps in the core (up to 70 m thick, red curves in Figure 5), pronounced thermohaline intrusions on the sides (not shown) and no double-diffusive staircases in the thermocline.

To gain further perspective on the data set, we examine monthly climatological data from the decade 2002–2013 (WOA13) and Mercator Ocean operational outputs.

5. Perspective From WOA13 Climatology and Mercator Ocean Operational Model

5.1. Comparison With the 2005–2012 WOA13 Climatology

We temporally (month by month) and spatially collocated WOA13 monthly climatologies with the IAOOS drift then interpolated the climatological profiles to the vertical resolution of the IAOOS data. Data shallower than 20 m are not considered. Differences are computed as $\text{data}_{\text{IAOOS}} - \text{data}_{\text{WOA13}}$ and are presented in scatter plots for three regions in Figure 9. We distinguish three layers: a near-surface layer, a thermocline and halocline layer, and a warm MAW layer (see Figure 9 caption for details).

Major differences in conservative temperatures are observed in the thermocline and upper MAW layer, with a general warming reaching values up to +0.75 °C in the Nansen Basin, +0.5 °C above the Gakkel Ridge and +0.3 °C in the Amundsen Basin (Figures 9a–9c). This warming is associated to a salinification on the order of +0.25 g/kg (Figures 9d–9f). On the other hand, the warmest and deeper part of the sampled MAW layer (~350 m) does not show this warming trend. These changes are the signature of the shoaling of the AW layer upper boundary. Polyakov et al. (2017) described a 40-m shoaling of the AW in the eastern Eurasian Basin between 2003 and 2015. Similarly, in the western Eurasian Basin, we document an average shoaling of the AW layer upper boundary (27.7-kg/m^3 isopycnal) of 22 m between 2005–2012 and 2017 (not shown). Figure 9h shows that at 145 m, temperatures on the order of ~1 °C are located further North in the 2017 data set than in the 2005–2012 climatology.

Furthermore, while surface temperatures show little variation, IAOOS 2017 surface salinities exhibit a significant fresh evolution when compared to the 2005–2012 WOA13 climatology (Figures 9d–9f). In the 2017 observations, the frontal region between Makarov and Eurasian waters is at 88.2°N, 10°E in April. The same frontal region in WOA13 in April appears further west than in the observations by about 40° (Figure 9g). This difference appears to be mainly responsible for the large surface salinity difference in the Amundsen Basin (Figure 9d). In WOA13, the frontal region varies in intensity and location from month to month (not shown): The freshest conditions near the North Pole are reached in September after summer sea ice melt, corresponding to a position of the frontal region comparable to the April 2017 observations (Figure 9g).

Korhonen et al. (2013) analyzed the evolution of pan-Arctic hydrographic properties over the 1991–2011 period. They observed a clear warming of the AW layer in the Eurasian Basin, mostly confined to the Nansen Basin (~+0.3 °C per decade). Our results indicate a reduced warming rate within the AW layer of +0.05 °C in the Eurasian Basin between 2005–2012 and 2017. The shoaling of the AW we observed between 2005 and 2012 and 2017 is consistent with the thickening of the AW layer (about 18 to 22 m per decade) described in Korhonen et al. (2013).

Rabe et al. (2014) pointed out to an Arctic-wide freshening of the upper layer between 1992 and 2012 with an overall salinity decrease of −0.6 g/kg. Peralta-Ferriz and Woodgate (2015) showed that the Eurasian Basin mixed layer freshened by ~−0.7 g/kg per decade from 1979 to 2012. Our results are consistent with a continuation of the freshening at the same rate between the 2005–2012 decade and 2017 (Figures 9d and 9f).

5.2. Mercator Ocean Operational System: Comparison to IAOOS 2017 Observations

The daily Mercator Ocean analyses are collocated in space and time with the IAOOS profiler data and interpolated to the data vertical resolution (Figures 10a and 10b). Temperature and salinity show a global agreement with the daily averaged observations, with a remarkably well located 27.7-kg/m^3 isopycnal (characterizing the top of the MAW and AW layer) and well-positioned AW mesoscale structures (Figures 10a and 10b).

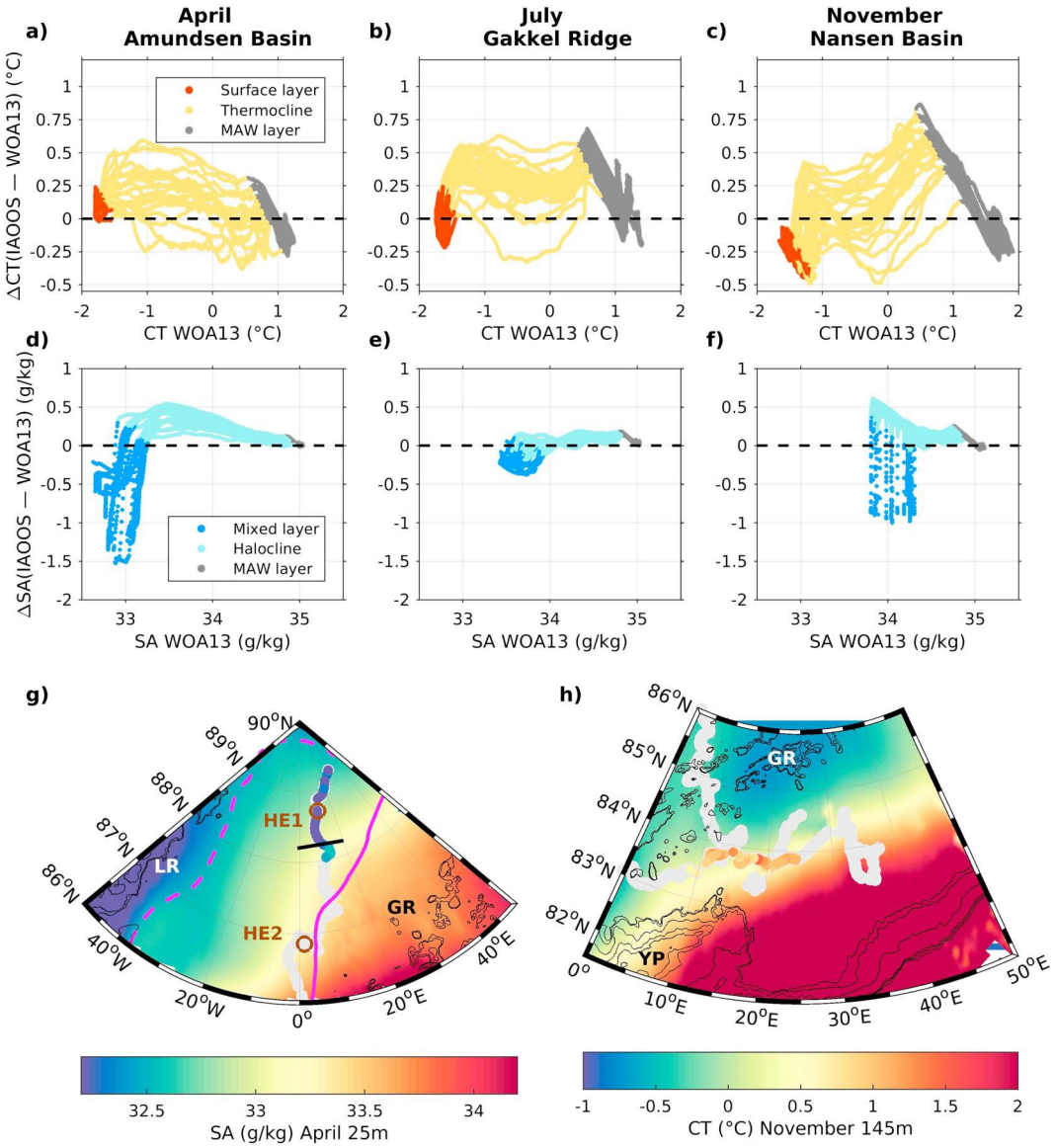

Figure 9. (a–f) Scatter plots of differences between Ice Atmosphere Ocean Observing System (IAOOS) observations and collocated WOA13 climatological data, in the Amundsen Basin (April, left panels), above the Gakkel Ridge (July, middle panels), and in the Nansen Basin (November, right panels). (a–c) Conservative temperature (°C). Red markers correspond to the isothermal near-surface layer ($CT \leq CT_{surf} + 0.2^{\circ}C$). Yellow markers represent the thermocline. Gray markers indicate the homogeneous Modified Atlantic Water layer (such as $|\partial_z T| \sim 0$ and $|\partial_z S| \sim 0$). (d–f) Absolute salinity (g/kg). Dark blue markers correspond to the mixed layer (down to the depth of N^2_{max}). Cyan markers correspond to the halocline. (g) Absolute salinity (g/kg) at 25 m in April and (h) conservative temperature (°C) at 145 m in November. Background is WOA13 2005–2012 climatology, and markers are IAOOS 2017 observations. Magenta lines in (g) are the 32.5 g/kg isohaline, representative of the frontal zone, in April (solid line) and September (dashed line) in the WOA13 2005–2012 climatology. Bathymetry isolines are in the thin black lines. GR, LR, and YP stand for Gakkel Ridge, Lomonosov Ridge, and Yermak Plateau, respectively.

However, the sections of model-observation differences (Figures 10c and 10d) reveal biases. The cold and slightly fresh bias at 150 m, larger in the Nansen Basin close to Fram Strait (−1.5 °C and −0.2 g/kg in November), results from an overly deep representation of the thermocline and MAW layer. A major bias in salinity (>1 g/kg) is observed in the surface layer near the North Pole (beginning of the time series; Figures 10b and 10c). The salinity bias (>0.5 g/kg^3) in the surface layer starting in November accompanies excessive sea ice formation in the model compared to the observations. The formation and deepening of the

NSTM in the model are consistent with observations, however the model NSTM is cooler (~−0.15 °C) and fresher (~−1 g/kg) than observed. In the western Fram Strait-Greenland slope region, a large patch of AW is visible in the model outputs (Figures 9 and 10). A plausible explanation is that the platforms drifted close to the AW recirculation branch in Fram Strait and the edge of this branch is likely rendered somewhat further west in the model outputs.

The first AW mesoscale structure (AW1) in the Nansen Basin is well located. In the model, AW1 is too warm (+0.5 °C; Figures 10c and 10e) and its bottom edge is located about 100 m deeper than in the observations (360-m depth in the model whereas 250-m depth in the observations; Figures 10a and 10e). The second mesoscale structure (AW2), close to Fram Strait, is not exactly at the same location as in the observations, leading to a large dipole-like difference in temperature and salinity (Figures 10c and 10d).

In summary, in spite of biases, the model is generally in good agreement with the observations and represents well the AW. We therefore use the model to investigate the origin and evolution of the AW mesoscale structures.

5.3. Observed Mesoscale Structures: Insights From Mercator Ocean System

5.3.1. Halocline Eddies

Mercator Ocean outputs have a significant salinity bias in the upper layer of the Amundsen Basin during the buoy sampling time (April–May), and the frontal region between the fresher Canadian waters and saltier Eurasian waters is represented much further west than the observations do at that time, by about 20° (Figure 11a). However, as in WOA13 the position of the frontal region in September in the model is further east and thus more comparable to the April observations (thin vs. dashed lines in Figure 11a). In Mercator Ocean outputs, the frontal region sheds numerous near-surface eddies in September. An example of an eddy occurring near the trajectory of the buoy during this chosen month is shown in Figures 11b–11d. While the modeled anticyclonic eddy occurs later in the year than the observed eddies HE1 and HE2 (September rather than April), their temperature, salinity and N^2 are quite similar (Figures 11b–11d). This suggests that halocline eddies HE1 and HE2 probably resulted from instabilities of the surface front. The modeled eddies have slightly larger radii (~20 km) than those observed (12 km) and are rather short-lived (4–18 weeks), as the model grid ((1/12)°) cannot resolve the mixed layer deformation radius (about 4 km; Brannigan et al., 2017).

5.3.2. AW Mesoscale Structures

The AW mesoscale structures in the model show great coherence with the observations. The first AW structure (AW1) crossed by the platforms (at 83.5°N, 35°E) is particularly well represented in the Mercator Ocean outputs. Model snapshots (Figure 12) reveal that it is likely an AW meander being shed from the Arctic Circumpolar Boundary Current, which later turned into an AW eddy. Model outputs indicate that the meander formed in late September. It detached from the boundary current by mid-November 2017 (at 83.7°N, 34.5°E) to form an anticyclonic AW eddy. The model suggests a radius ~30 km, significantly larger than the Rossby deformation radius R_d in this area (R_d on the order of 10 km). In the model outputs, the eddy is characterized by salinity in the range 35.06–35.11 g/kg and temperature between 2 and 2.7 °C in its core, consistent with observations (Figure 10), and a maximum azimuthal speed of 2.5 cm/s at its edge (Figure 12). Model outputs show a slightly northwestward propagation for 2.5 months until late January 2018 (at 83.85°N, 34°E) when the rotation decays (Figure 12). In March 2018, the rotating motion disappears and the T-S characteristics are eroded due to mixing with the surrounding water (Figure 12i).

To examine the performance of the Mercator Ocean operational model regarding AW eddies in the region, we compare model outputs to an AW anticyclonic eddy extensively described by Våge et al. (2016). The eddy was encountered in September 2012 above the shelf slope of Kvitøya Through (81.75°N, 30°E) and has a radius $R \sim 10$–15 km, comparable with R_d. Its core was warmer (2–3.3 °C) and saltier (35.08–35.2 g/kg) than AW1. The maximum azimuthal speed at the edge of the eddy is ~7 cm/*S.* Mercator Ocean outputs reproduce the AW eddy described by Våge et al. (2016) remarkably well (not shown) in particular its location, temperature, salinity, and core depth (~250 m) at the precise date (21 September 2012). The model exhibits an azimuthal speed of ~5 cm/s somewhat smaller than the observations by $\Delta|u| \sim -2$ cm/s, falling within the acoustic Doppler current profiler instrument error (±2 cm/s; Våge et al., 2016). The simulated eddy radius and bottom edge depth are on the order of the observations, even if slightly overestimated (respectively $\Delta R \sim +15$ km and $|\Delta z| > +200$ m). Indeed, as mentioned above, the model grid resolution (about 6 km in

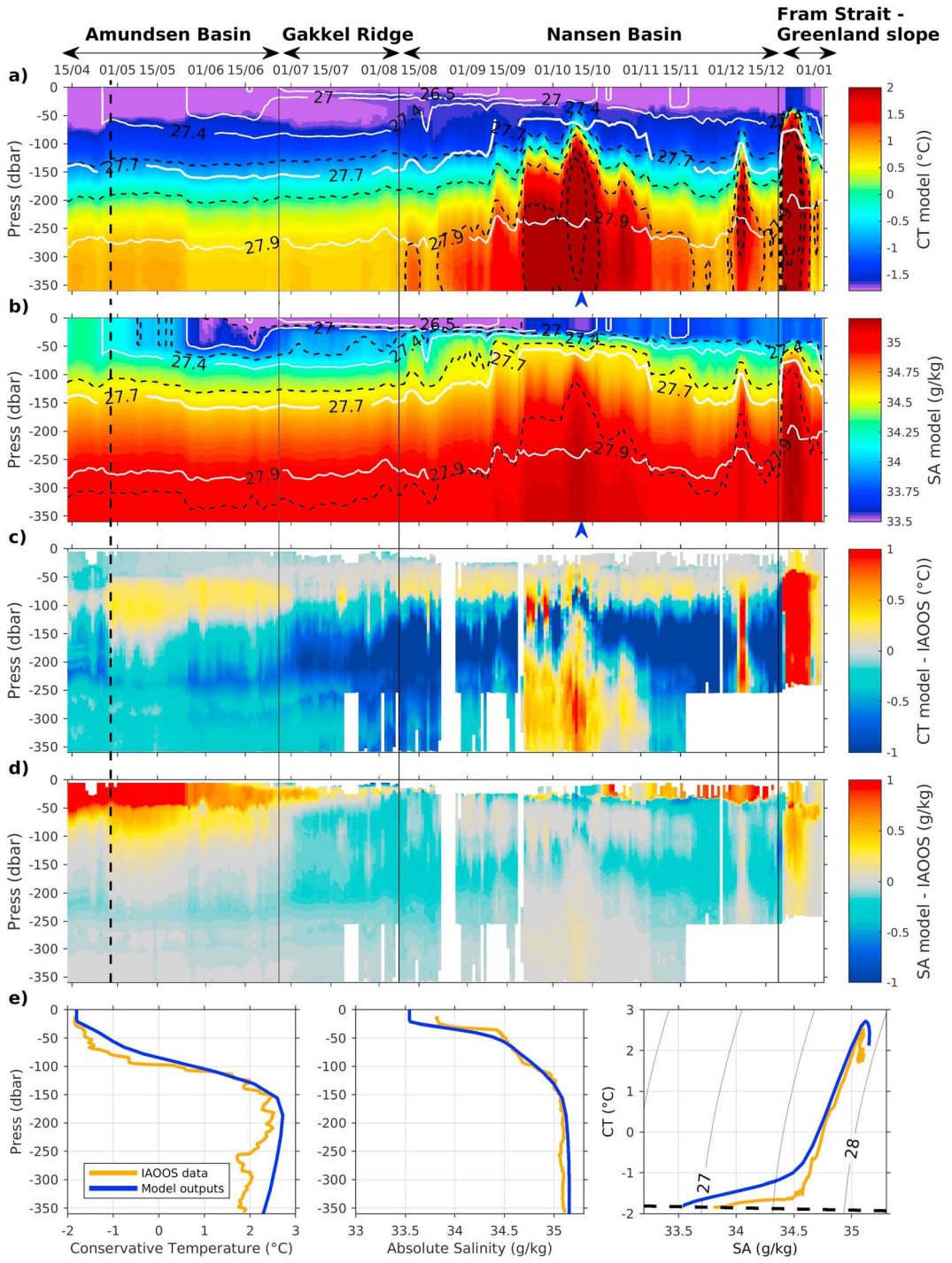

Figure 10. (a) Conservative temperature (°C) and (b) absolute salinity (g/kg) from daily Mercator Ocean model outputs collocated with the platform drift and interpolated to the data vertical resolution. Black dashed lines are temperature and salinity isolines in the model. Thin white lines are isopycnals. The thick white line is the 27.7-kg/m^3 isopycnal. The four regions are indicated as in Figure 3. Differences between model outputs and Ice Atmosphere Ocean Observing System observations in (c) conservative temperature (°C) and (d) absolute salinity. (e) CT, SA profiles, and associated TS diagram in observations (yellow) and model outputs (blue) at the time of AW1 (blue arrow on 7 October under panels a and b).

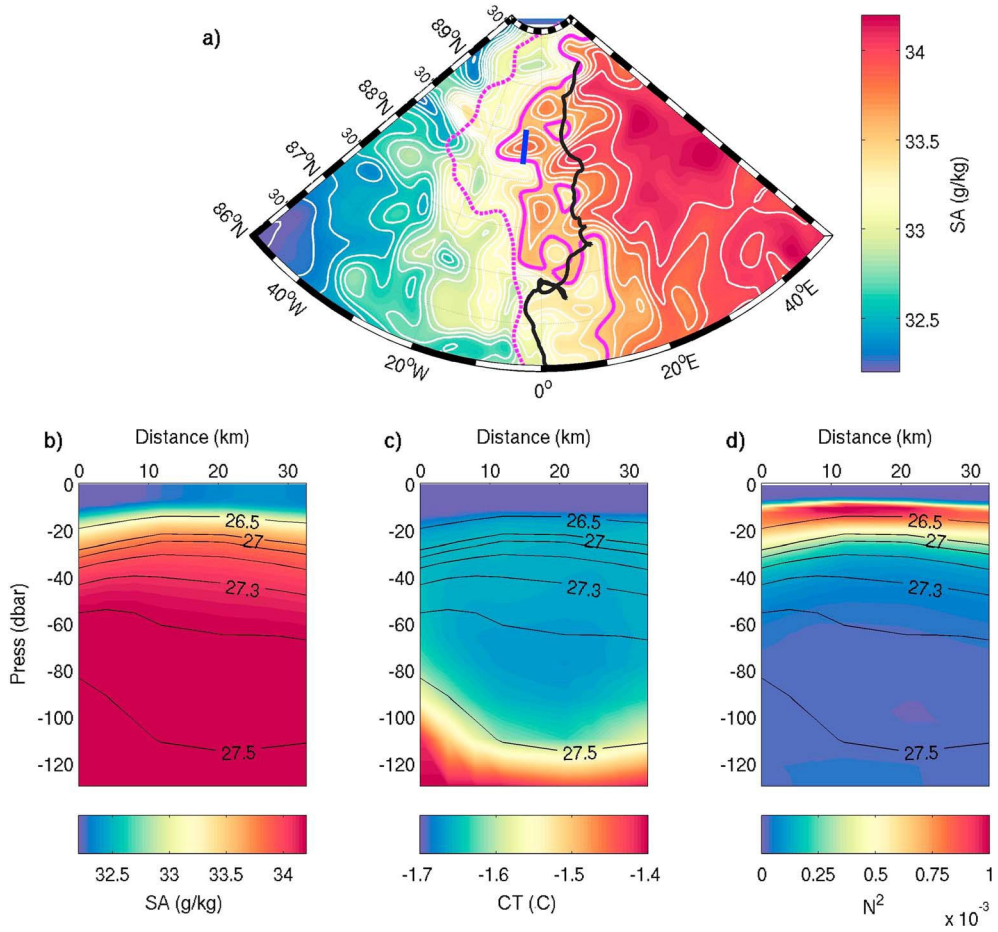

Figure 11. (a) Mercator Ocean salinity (SA) field at 25-m depth on 4 September 2017, with white isolines every 0.1 g/kg. The buoy trajectory is shown in black, and the location of the eddy section in blue. As the model exhibits a large salinity bias near the North Pole (>1 g/kg^3), the 33.5-g/kg isoline (magenta lines) is considered representative of the frontal zone instead of 32.5 g/kg in Figure 9. Its position on 4 September (solid) is reported, as well as in April (dashed) when the buoy was in this region. (b–d) Sections through the anticyclonic eddy and along the blue line in (a) from south to north, depicting (b) absolute salinity (g/kg), (c) conservative temperature (°C), and (d) Brunt-Väisälä frequency (N^2), with isopycnal contours overlayed in black.

the area) is too large to resolve explicitly the Rossby deformation radius. Hence, the simulated eddies have necessarily radii $R \geq R_d$.

AW2 is encountered at 82.8°N, 3°W between 12 and 22 December 2017 (Figures 2 and 3). In the model, the AW recirculation branch represented between 20 and 30 December 2017 at 81°N, 4°W to 82.7°N, 4°W (Figure 10) shows very similar T-S properties to AW2 observed close by, suggesting that AW2 is an AW recirculation branch.

6. Summary and Discussion

The 8-month-long physical and biogeochemical data set documented the upper 350 m of four regions with distinct hydrographic characteristics in the Western Eurasian Arctic Basin (summarized in Table 2).

The IAOOS 2017 campaign provided new insights on the recent state of the Arctic western Eurasian Basin. High CDOM and low nitrate in the upper Amundsen Basin allowed the backtracking of the water mass as shelf-origin water, enriched in Siberian river runoff and carried by the TPD across the central Arctic Basin (Damm et al., 2018; Kipp et al., 2018).

Comparison with WOA13 climatology indicates a shallower AW layer in 2017 than over the 2005–2012 period in the western Eurasian Basin, consistent with the thickening of the AW layer described in Korhonen

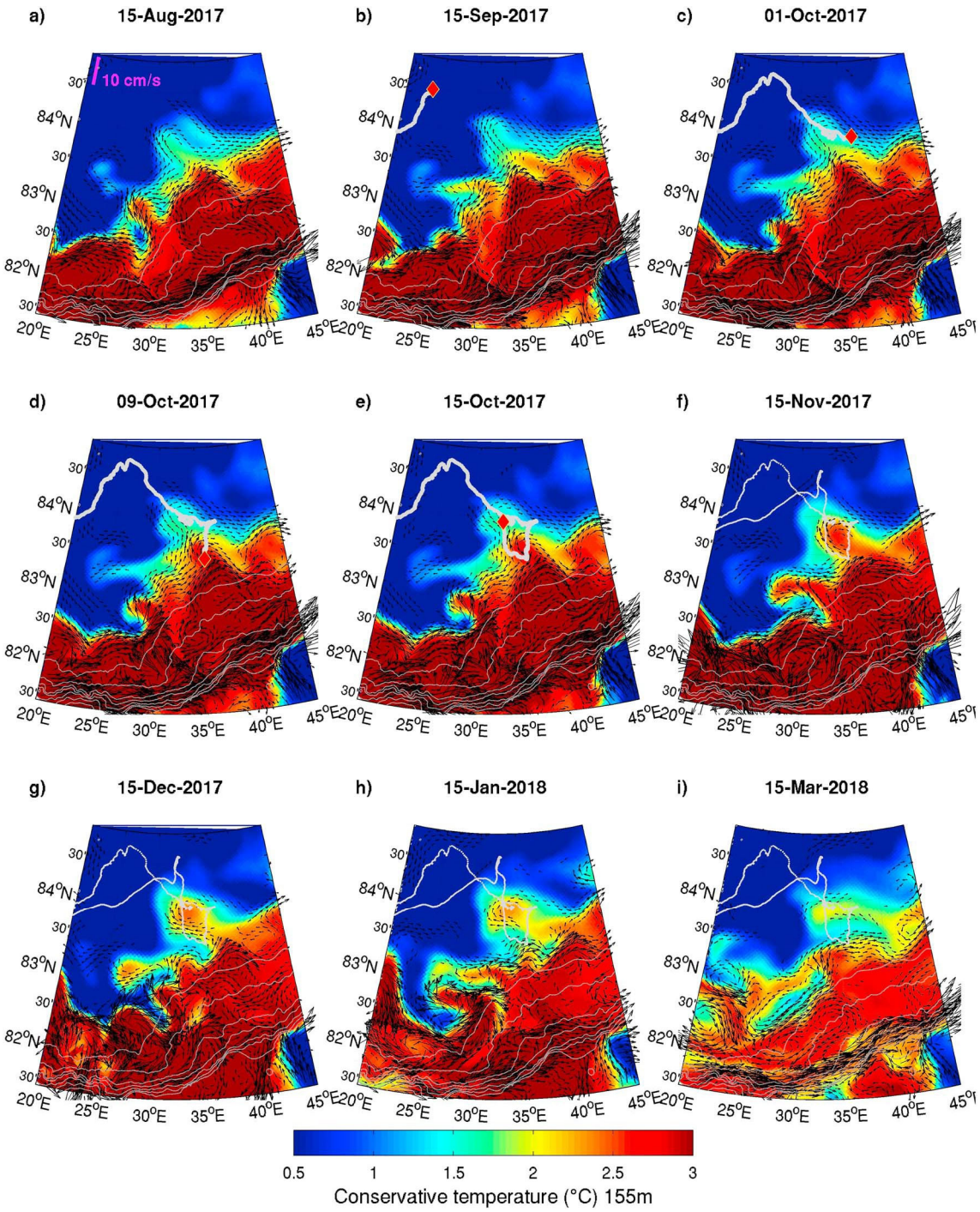

Figure 12. Selected snapshots of the Atlantic Water mesoscale structure in Mercator Ocean model outputs shown at 155 m. The white line corresponds to the Ice Atmosphere Ocean Observing System platforms trajectory. The red diamond marks the position of the platforms at each selected date. Gray isolines are bathymetry contours. Black arrows are the current at 155 m in the model; the scale is indicated in (a). Velocities lower than 1 cm/s are not shown.

et al. (2013). Polyakov et al. (2017) showed that this shoaling of the AW layer, together with the sea ice decline and weakened halocline, are the symptoms of the progressive Atlantification of the Eurasian Basin. In 2017, the mixed layer is fresher than in 2005–2012, indicating the continuation of the freshening described in Rabe et al. (2014) and Peralta-Ferriz and Woodgate (2015). Coincidently, the frontal zone at the confluence of fresher surface water from the Makarov Basin and saltier Eurasian surface water appears to have shifted further southeast (near 88.2°N, 10°E) compared to 2005–2012 (near 88.5°N, 45°E).

Alkire et al. (2015) point out the large interannual variability in surface salinity in the central Arctic, partly attributed to shifts in the alignment of the TPD. Several studies document the contribution of the Arctic Oscillation index in the shifts of the TPD and Arctic general surface circulation (Alkire et al., 2015; Armitage et al., 2018; Morison et al., 2012). However, the relationship between Arctic Oscillation and river runoff pathways in the present data set remains unclear.

The IAOOS platforms documented mesoscale structures within the halocline as well as in the warm layer during their drift through the Arctic Eurasian Basin. Two anticyclonic halocline eddies are identified in the Amundsen Basin, near 87°N, 5°E and 89°N, 8°E, respectively, with radii R_{HE} ~ 12 km (~R_d in the region). They carry surface water properties (colder temperature ΔT ~ 0.15 °C, oxygen-enriched ΔAOU ~ −25 μmol/kg and nitrate-depleted ΔNO^-_3 ~ −1.5 μmol/kg) despite salinities similar to their environment (S ~ 33.75 g/kg). Mercator Ocean model outputs suggest that these halocline eddies probably resulted from instabilities in the surface front between the fresher Makarov waters and saltier Eurasian waters. However, while Timmermans et al. (2008) and Zhao et al. (2014) observed such halocline eddies with lifetimes from months to years, the modeled eddies have slightly larger radii (~20 km) and are rather short-lived (4–18 weeks), as the model grid cannot resolve the mixed layer deformation radius (about 4 km). However, as far as we know it is the first time that such halocline eddies in the central Arctic Basin have been reproduced in a model.

Two AW mesoscale structures were encountered in the Nansen Basin. They exhibit cores of AW with temperatures larger than 2 °C and salinities larger than their environment (ΔS ~ + 0.1–0.2 g/kg). They are oxygen enriched compared to their environment and slightly nitrate depleted. One AW structure was encountered north of the Yermak Plateau in December 2017 (near 83°N, 1°W). Even though this structure is not reproduced at the same time and location in the model, the Mercator Ocean outputs have provided evidence that is it likely an AW recirculating branch, circulating back toward the Fram Strait. The large AW structure, crossed in October 2017 unusually northeast in the Nansen Basin (at 83.5°N, 35°E), is particularly well represented in the model and identified as a meander of AW detaching from the Arctic Circumpolar Boundary Current. The model outputs suggest that the AW meander turned into an anticyclonic AW eddy about a month after the platforms drifted away, propagating slightly northwestward for 2.5 months until reaching 83.7°N, 34.5°E in February 2018.

Comparisons with an eddy documented by Våge et al. (2016) underlined the good performance of the (1/12)° Mercator Ocean model in representing AW eddies. However, the (1/12)° horizontal resolution grid is only eddy permitting in the Eurasian Basin, with a spatial resolution of ~4 km in the area. These limitations are likely to prevent the detection of smaller sized eddies and eddy tracking in the Basin interior. Crews et al. (2017) provided a first fine resolution (800 m × 800 m) model-based quantitative survey of eddy-mediated transport of AW from the boundary current to the Eurasian Basin. 177 eddies in 2 years were detected on the Svalbard continental shelf, but the large majority (98%) stayed south of 83°N, as in the Mercator Ocean model. To our knowledge, it is the first time that an AW meander is documented as far as 83.5°N, 35°E in the Nansen Basin interior.

Several studies suggest that eddies have a significant influence on the lateral current-to-basin interior exchanges of heat, salt, tracers, and nutrients (Mathis et al., 2007; Nishino et al., 2011; Zhao et al., 2014). Mathis et al. (2007) and Nishino et al. (2011) indicate that in the Canada Basin, eddies are likely major nutrients providers to the upper layer. Here, measurements within the AW meanders and eddies crossed in autumn-winter 2017 suggest a possible similar input of nutrients in the Eurasian Basin upper layer.

This study highlights the recent physical changes in the western Eurasian Basin. In this increasingly ice-free ocean, the fresher surface water and shallower warm AW layer are likely to have significant impacts on the biogeochemistry of the Arctic Ocean (Arrigo & van Dijken, 2015; Bluhm et al., 2015; Timmermans et al., 2010). These will be discussed in a forthcoming paper presenting the biogeochemical observations and near-surface pCO_2 evolution from IAOOS 2017 data.

Appendix A: Estimation of the Minimum Internal Wave Amplitude

Despite the nonadapted sampling frequency of the IAOOS platforms (every 12 hr), we suggest that the IAOOS data can provide an estimate of the minimum internal wave amplitude in the still sparsely documented Eurasian Basin, following the method described in Dosser et al. (2014).

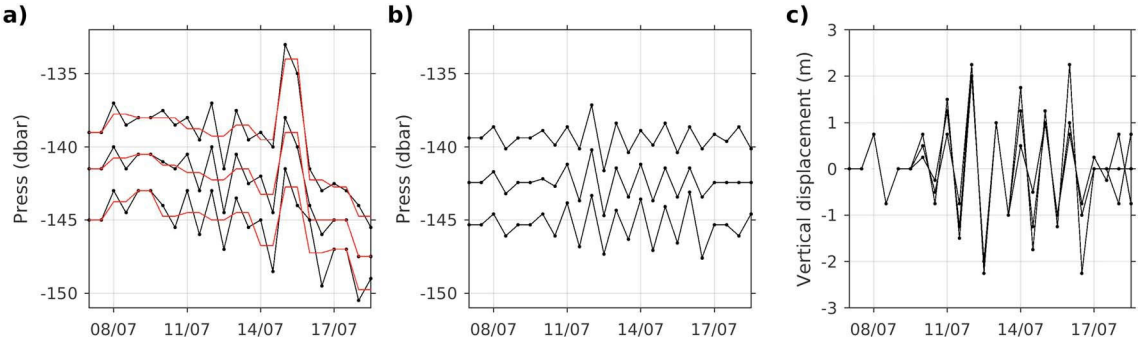

Figure A1. (a) Example of three sample isopycnals over a 12-day period (7 to 18 July 2017, over the Gakkel Ridge). The black lines show the depth of the isopycnals, and the red line shows the daily mean depth of the three isopycnals. (b) The same isopycnals with the mean removed, leaving only displacements near the inertial frequency. (c) Vertical displacements of the three isopycnals combined to maximize the number of points available.

Vertical displacements of isopycnals are estimated by tracking density surfaces, originally regularly distributed (each 3 m) in the first profile, along the drift (Figure A1a). Near-inertial waves typically have horizontal wavelengths on the order of kilometers and vertical wavelengths on the order of 10–100 m. For each isopycnal, the daily mean is removed. Vertical displacements are combined with those of the isopycnals immediately above and below, tripling the number of available data points per estimate and reducing the impact of random noise (Figure A1b). The estimation of isopycnals depths is limited by instrument noise and vertical resolution (~1 m); thus, vertical displacements smaller than 1 m were not considered. This implies that the present estimation does not apply to the quiescent Amundsen Basin, where displacements do not exceed the 1-m limit. In the end, we estimated the minimum near-inertial internal wave amplitude to be ~2 m above and south of the Gakkel Ridge in the upper 350 m of the Eurasian Basin (Figure A1c).

Acknowledgments
We are deeply grateful to the many people who participated to the development and tests of the biogeochemical profiler at Ifremer facilities in Brest (France) and during the N-ICE 2015 ice camp from RV Lance north of Svalbard: Magali Garracio, Antoine Guillot, Christine Drezen and Michel Calzas, Nicolas Villacieros Robineau, Jean-Philippe Savy, and Victoire Rérolle. We thank Matthieu Labaste, Victoire Rérolle, and Sergey Pisarev for their contribution to the preparation and deployment of the IAOOS platforms form the North Pole in April 2017. Magali Garracio was essential to the data recovery and decoding processes. Discussions with Catherine Schmechtig on the data processing are gratefully acknowledged. Véronique Garçon and Carole Barus contributed to the addition of the Rem-A package to the profiler. The development and field work were funded through the ANR EQUIPEX IAOOS project through ANR-10-EQX-32-01 grant and the ICE-ARC programme from the European Union 7th Framework Programme, grant 603887. Marylou Athanase, Zoe Koenig, and Elisabeth Boles were supported through the Pan Arctic Options Belmont Forum project (ANR-14-AORS-003-01). Profiler data are available at SEANOE (https://doi.org/10.17882/57288). The model outputs are available at Copernicus Marine Environment Monitoring Service (CMEMS; http://marine.copernicus.eu/). We are deeply grateful to Editor Laurence Padman and two anonymous reviewers for their thorough comments, which helped us improve the manuscript.

References

Alkire, M. B., Morison, J., & Andersen, R. (2015). Variability in the meteoric water, sea-ice melt, and Pacific water contributions to the central Arctic Ocean, 2000–2014. *Journal of Geophysical Research: Oceans*, *120*, 1573–1598. https://doi.org/10.1002/2014JC010023

Armitage, T. W. K., Bacon, S., & Kwok, R. (2018). Arctic sea level and surface circulation response to the Arctic Oscillation. *Geophysical Research Letters*, *45*, 6576–6584. https://doi.org/10.1029/2018GL078386

Arrigo, K. R., & van Dijken, G. L. (2015). Continued increases in Arctic Ocean primary production. *Progress in Oceanography*, *136*, 60–70. https://doi.org/10.1016/j.pocean.2015.05.002

Bebieva, Y., & Timmermans, M. L. (2016). An examination of double-diffusive processes in a mesoscale eddy in the Arctic Ocean. *Journal of Geophysical Research: Oceans*, *121*, 457–475. https://doi.org/10.1002/2015JC011105

Bluhm, B. A., Kosobokova, K. N., & Carmack, E. C. (2015). A tale of two basins: An integrated physical and biological perspective of the deep Arctic Ocean. *Progress in Oceanography*, *139*, 89–121. https://doi.org/10.1016/j.pocean.2015.07.011

Brannigan, L., Johnson, H., Lique, C., Nycander, J., & Nilsson, J. (2017). Generation of subsurface anticyclones at Arctic surface fronts due to a surface stress. *Journal of Physical Oceanography*, *47*(11), 2653–2671. https://doi.org/10.1175/JPO-D-17-0022.1

Carmack, E., Polyakov, I., Padman, L., Fer, I., Hunke, E., Hutchings, J., Jackson, J., et al. (2015). Toward quantifying the increasing role of oceanic heat in sea ice loss in the new Arctic. *Bulletin of the American Meteorological Society*, *96*(12), 2079–2105. https://doi.org/10.1175/BAMS-D-13-00177.1

Codispoti, L. A., Kelly, V., Thessen, A., Matrai, P., Suttles, S., Hill, V., et al. (2013). Synthesis of primary production in the Arctic Ocean: III. Nitrate and phosphate-based estimates of net community production. *Progress in Oceanography*, *110*, 126–150. https://doi.org/10.1016/j.pocean.2012.11.006

Comiso, J. C., Parkinson, C. L., Gersten, R., & Stock, L. (2008). Accelerated decline in the Arctic sea ice cover. *Geophysical Research Letters*, *35*, L01703. https://doi.org/10.1029/2007GL031972

Crews, L., Sundfjord, A., Albretsen, J., & Hattermann, T. (2017). Mesoscale eddy activity and transport in the Atlantic Water inflow region north of Svalbard. *Journal of Geophysical Research: Oceans*, *123*, 201–215. https://doi.org/10.1002/2017JC013198

Dai, A., Qian, T., Trenberth, K. E., & Milliman, J. D. (2009). Changes in continental freshwater discharge from 1948 to 2004. *Journal of Climate*, *22*(10), 2773–2792. https://doi.org/10.1175/2008JCLI2592.1

Damm, E., Bauch, D., Krumpen, T., Rabe, B., Korhonen, M., Vinogradova, E., & Uhlig, C. (2018). The Transpolar Drift conveys methane from the Siberian Shelf to the central Arctic Ocean. *Scientific Reports*, *8*(1), 4515. https://doi.org/10.1038/s41598-018-22801-z

Dmitrenko, I. A., Kirillov, S. A., Ivanov, V. V., & Woodgate, R. A. (2008). Mesoscale Atlantic water eddy off the Laptev Sea continental slope carries the signature of upstream interaction. *Journal of Geophysical Research*, *113*, C07005. https://doi.org/10.1029/2007JC004491

Dosser, H. V., Rainville, L., & Toole, J. M. (2014). Near-inertial internal wave field in the Canada Basin from ice-tethered profilers. *Journal of Physical Oceanography*, *44*(2), 413–426. https://doi.org/10.1175/JPO-D-13-0117.1

Good, S. A., Martin, M. J., & Rayner, N. A. (2013). EN4: Quality controlled ocean temperature and salinity profiles and monthly objective analyses with uncertainty estimates. *Journal of Geophysical Research: Oceans*, *118*, 6704–6716. https://doi.org/10.1002/2013JC009067

Jackson, J. M., Carmack, E. C., McLaughlin, F. A., Allen, S. E., & Ingram, R. G. (2010). Identification, characterization, and change of the near-surface temperature maximum in the Canada Basin, 1993–2008. *Journal of Geophysical Research*, *115*, C05021. https://doi.org/10.1029/2009JC005265

Jackson, K., Wilkinson, J., Maksym, T., Meldrum, D., Beckers, J., Haas, C., & Mackenzie, D. (2013). A novel and low-cost sea ice mass balance buoy. *Journal of Atmospheric and Oceanic Technology*, *30*(11), 2676–2688. https://doi.org/10.1175/JTECH-D-13-00058

Jeffries, M. O., Overland, J. E., & Perovich, D. K. (2013). The Arctic. *Physics Today*, *66*(10), 35–40. https://doi.org/10.1063/PT.3.2147

Johnson, K., Pasqueron De Fommervault, O., Serr, R., D'Ortenzio, F., Schmechtig, C., Claustre, H., & Poteau, A. (2018). Processing Bio-Argo nitrate concentration at the DAC Level. Version 1.1, March 3rd 2018. IFREMER for Argo Data Management (22 pp.). https://doi.org/10.13155/46121

Kipp, L. E., Charette, M. A., Moore, W. S., Henderson, P. B., & Rigor, I. G. (2018). Increased fluxes of shelf-derived materials to the central Arctic Ocean. *Science Advances*, *4*(1), eaao1302. https://doi.org/10.1126/sciadv.aao1302

Koenig, Z., Provost, C., Villacieros- Robineau, N., Sennechael, N., & Meyer, A. (2016). Winter ocean-ice interactions under thin sea ice observed by IAOOS platforms during N-ICE2015: Salty surface mixed layer and active basal melt. *Journal of Geophysical Research: Oceans*, *121*, 7898–7916. https://doi.org/10.1002/2016JC012195

Koenig, Z., Provost, C., Villacieros- Robineau, N., Sennechael, N., Meyer, A., Lellouche, J.-M., & Garric, G. (2017). Atlantic waters inflow north of Svalbard: Insights from IAOOS observations and Mercator Ocean global operational system during N-ICE2015. *Journal of Geophysical Research: Oceans*, *122*, 1254–1273. https://doi.org/10.1002/2016JC012424

Korhonen, M., Rudels, B., Marnela, M., Wisotzki, A., & Zhao, J. (2013). Time and space variability of freshwater content, heat content and seasonal ice melt in the Arctic Ocean from 1991 to 2011. *Ocean Science*, *9*(6), 1015–1055. https://doi.org/10.5194/os-9-1015-2013

Krishfield, R., Toole, J., Proshutinsky, A., & Timmermans, M. L. (2008). Automated ice-tethered profilers for seawater observations under pack ice in all seasons. *Journal of Atmospheric and Oceanic Technology*, *25*(11), 2091–2105. https://doi.org/10.1175/2008JTECHO587.1

Laney, S. R., Krishfield, R. A., Toole, J. M., Hammar, T. R., Ashjian, C. J., & Timmermans, M. L. (2014). Assessing algal biomass and bio-optical distributions in perennially ice-covered polar ocean ecosystems. *Polar Science*, *8*(2), 73–85. https://doi.org/10.1016/j.polar.2013.12.003

Lellouche, J. M., Greiner, E., le Galloudec, O., Garric, G., Regnier, C., Drevillon, M., et al. (2018). Recent updates to the Copernicus Marine Service global ocean monitoring and forecasting real-time 1/ 12° high-resolution system. *Ocean Science*, *14*(5), 1093–1126. https://doi.org/10.5194/os-14-1093-2018

Locarnini, R. A., Mishonov, A. V., Antonov, J. I., Boyer, T. P., Garcia, H. E., Baranova, O. K., et al. (2013). World ocean atlas 2013, volume 1: Temperature. In S. A. M. Levitus & A. Mishonov (Eds.), *NOAA Atlas NESDIS 73* (40 pp.). https://doi.org/10.7289/V55X26VD

Madec, G. (2008). NEMO, the ocean engine, Note du Pole de modelisation, Institut Pierre-Simon Laplace (IPSL), France, no 27 ISSN no 1288–1619.

Mariage, V., Pelon, J., Blouzon, F., Victori, S., Geyskens, N., Amarouche, N., et al. (2017). Iaoos microlidar-on-buoy development and first atmospheric observations obtained during 2014 and 2015 Arctic drifts. *Optics Express*, *25*(4), A73–A84. https://doi.org/10.1364/OE.25.000A73

Mathis, J. T., Pickart, R. S., Hansell, D. A., Kadko, D., & Bates, N. R. (2007). Eddy transport of organic carbon and nutrients from the Chukchi shelf: Impact on the upper halocline of the western Arctic Ocean. *Journal of Geophysical Research*, *112*, C05011. https://doi.org/10.1029/2006JC003899

McDougall, T. J., Jackett, D. R., Millero, F. J., Pawlowicz, R., & Barker, P. M. (2012). A global algorithm for estimating absolute salinity. *Ocean Science*, *8*(6), 1123–1134. https://doi.org/10.5194/os-8-1123-2012

Morison, J., Kwok, R., Peralta-Ferriz, C., Alkire, M., Rigor, I., Andersen, R., & Steele, M. (2012). Changing Arctic ocean freshwater pathways. *Nature*, *481*(7379), 66–70. https://doi.org/10.1038/nature10705

Nishino, S., Itoh, M., Kawaguchi, Y., Kikuchi, T., & Aoyama, M. (2011). Impact of an unusually large warm-core eddy on distributions of nutrients and phytoplankton in the southwestern Canada Basin during late summer/early fall 2010. *Geophysical Research Letters*, *38*, L16602. https://doi.org/10.1029/2011GL047885

Onarheim, I. H., Smedsrud, L. H., Ingvaldsen, R. B., & Nilsen, F. (2014). Loss of sea ice during winter north of Svalbard. *Tellus A: Dynamic Meteorology and Oceanography*, *66*(1), 23933. https://doi.org/10.3402/tellusa.v66.23933

Peralta-Ferriz, C., & Woodgate, R. A. (2015). Seasonal and interannual variability of pan-Arctic surface mixed layer properties from 1979 to 2012 from hydrographic data, and the dominance of stratification for multiyear mixed layer depth shoaling. *Progress in Oceanography*, *134*, 19–53. https://doi.org/10.1016/j.pocean.2014.12.005

Perovich, D. K., Richter-Menge, J. A., Jones, K. F., Light, B., Elder, B. C., Polashenski, C., et al. (2011). Arctic sea-ice melt in 2008 and the role of solar heating. *Annals of Glaciology*, *52*(57), 355–359. https://doi.org/10.3189/172756411795931714

Pham, D. T., Verron, J., & Roubaud, M. C. (1998). A singular evolutive extended Kalman filter for data assimilation in oceanography. *Journal of Marine Systems*, *16*(3–4), 323–340. https://doi.org/10.1016/S0924-7963(97)00109-7

Polyakov, I. V., Padman, L., Lenn, Y. D., Pnyushkov, A., Rember, R., & Ivanov, V. V. (2018). Eastern Arctic Ocean diapycnal heat fluxes through large double-diffusive steps. *Journal of Physical Oceanography*, *2018*.

Polyakov, I. V., Pnyushkov, A. V., Alkire, M. B., Ashik, I. M., Baumann, T. M., Carmack, E. C., et al. (2017). Greater role for Atlantic inflows on sea-ice loss in the Eurasian Basin of the Arctic Ocean. *Science*, *356*(6335), 285–291. https://doi.org/10.1126/science.aai8204

Polyakov, I. V., Timokhov, L. A., Alexeev, V. A., Bacon, S., Dmitrenko, I. A., Fortier, L., et al. (2010). Arctic Ocean warming contributes to reduced polar ice cap. *Journal of Physical Oceanography*, *40*(12), 2743–2756. https://doi.org/10.1175/2010JPO4339.1

Provost, C., Pelon, J., Sennéchael, N., Calzas, M., Blouzon, F., Desautez, A., et al. (2015). IAOOS (ice-atmosphere-arctic ocean observing system, 2011-2019). *Mercator Ocean Quarterly Newsletter*, *51*, 13–15.

Provost, C., Sennéchael, N., Miguet, J., Itkin, P., Rösel, A., Koenig, Z., et al. (2017). Observations of flooding and snow-ice formation in a thinner arctic sea ice regime during the N-ICE2015 campaign: Influence of basal ice melt and storms. *Journal of Geophysical Research: Oceans*, *122*, 7115–7134. https://doi.org/10.1002/2016JC012011

Rabe, B., Karcher, M., Kauker, F., Schauer, U., Toole, J. M., Krishfield, R. A., et al. (2014). Arctic Ocean basin liquid freshwater storage trend 1992–2012. *Geophysical Research Letters*, *41*, 961–968. https://doi.org/10.1002/2013GL058121

Randelhoff, A., & Guthrie, J. D. (2016). Regional patterns in current and future export production in the central Arctic Ocean quantified from nitrate fluxes. *Geophysical Research Letters*, *43*, 8600–8608. https://doi.org/10.1002/2016GL070252

Rudels, B., Meyer, R., Fahrbach, E., Ivanov, V. V., Østerhus, S., Quadfasel, D., et al. (2000). Water mass distribution in Fram Strait and over the Yermak Plateau in summer 1997. *Annales Geophysicae*, *18*(6), 687–705. https://doi.org/10.1007/s00585-000-0687-5

Sakamoto, C. M., Johnson, K. S., & Coletti, L. J. (2009). Improved algorithm for the computation of nitrate concentrations in seawater using an in situ ultraviolet spectrophotometer. *Limnology and Oceanography: Methods*, *8*(6), 1123–1134. https://doi.org/10.5194/os-8-1123-2012

Schauer, U., Rudels, B., Jones, E. P., Anderson, L. G., Muench, R. D., Björk, G., et al. (2002). Confluence and redistribution of Atlantic water in the Nansen, Amundsen and Makarov basins. *Annales Geophysicae*, *20*(2), 257–273. https://doi.org/10.5194/angeo-20-257-2002

Serreze, M. C., & Barry, R. G. (2011). Processes and impacts of Arctic amplification: A research synthesis. *Global and Planetary Change*, *77*(1–2), 85–96. https://doi.org/10.1016/j.gloplacha.2011.03.004

Stroeve, J. C., Serreze, M. C., Holland, M. M., Kay, J. E., Malanik, J., & Barrett, A. P. (2012). The Arctic's rapidly shrinking sea ice cover: A research synthesis. *Climatic Change*, *110*(3–4), 1005–1027. https://doi.org/10.1007/s10584-011-0101-1

Sutherland, D. A., & Pickart, R. S. (2008). The East Greenland coastal current: Structure, variability, and forcing. *Progress in Oceanography*, *78*(1), 58–77. https://doi.org/10.1016/j.pocean.2007.09.006

Thierry V., Bittig, H., Gilbert, D., Kobayashi, T., Sato, K., & Schmid, C. (2016). Processing Argo OXYGEN data at the DAC level, v2.2. https://doi.org/10.13155/39795

Timmermans, M. L., Krishfield, R., Laney, S., & Toole, J. (2010). Ice-tethered profiler measurements of dissolved oxygen under permanent ice cover in the Arctic Ocean. *Journal of Atmospheric and Oceanic Technology*, *27*(11), 1936–1949. https://doi.org/10.1175/2010JTECHO772.1

Timmermans, M. L., Proshutinsky, A., Krishfield, R. A., Perovich, D. K., Richter-Menge, J. A., Stanton, T. P., & Toole, J. M. (2011). Surface freshening in the Arctic Ocean's Eurasian Basin: An apparent consequence of recent change in the wind-driven circulation. *Journal of Geophysical Research*, *116*, C00D03. https://doi.org/10.1029/2011JC006975

Timmermans, M. L., Toole, J., Proshutinsky, A., Krishfield, R., & Plueddemann, A. (2008). Eddies in the Canada Basin, Arctic Ocean, observed from ice-tethered profilers. *Journal of Physical Oceanography*, *38*(1), 133–145. https://doi.org/10.1175/2007JPO3782.1

Toole, J. M., Timmermans, M. L., Perovich, D. K., Krishfield, R. A., Proshutinsky, A., & Richter-Menge, J. A. (2010). Influences of the ocean surface mixed layer and thermohaline stratification on Arctic Sea ice in the central Canada Basin. *Journal of Geophysical Research*, *115*, C10018. https://doi.org/10.1029/2009JC005660

Våge, K., Pickart, R. S., Pavlov, V., Lin, P., Torres, D. J., Ingvaldsen, R., Sundfjord, A., et al. (2016). The Atlantic Water boundary current in the Nansen Basin: Transport and mechanisms of lateral exchange. *Journal of Geophysical Research: Oceans*, *121*, 6946–6960. https://doi.org/10.1002/2016JC011715

Zhao, M., Timmermans, M. L., Cole, S., Krishfield, R., Proshutinsky, A., & Toole, J. (2014). Characterizing the eddy field in the Arctic Ocean halocline. *Journal of Geophysical Research: Oceans*, *119*, 8800–8817. https://doi.org/10.1002/2014JC010488

Zweng, M. M., Reagan, J. R., Antonov, J. I., Locarnini, R. A., Mishonov, A. V., Boyer, T. P., et al. (2013). World ocean atlas 2013, volume 2: Salinity. In S. A. M. Levitus & A. Mishonov (Eds.), *NOAA Atlas NESDIS 74* (39 pp.).